Contributions to Mineralogy and Petrology

# Textural and chemical evolution of pyroxene during hydration and deformation: a consequence of retrograde metamorphism.

--Manuscript Draft--

| | |
|---|---|
| **Manuscript Number:** | |
| **Full Title:** | Textural and chemical evolution of pyroxene during hydration and deformation: a consequence of retrograde metamorphism. |
| **Article Type:** | Original Paper |
| **Keywords:** | Granulite; Amphibolite; Fluid; Stress; Strain |
| **Corresponding Author:** | Centrella Stephen<br>Institut für Mineralogie<br>Münster, GERMANY |
| **Corresponding Author Secondary Information:** | |
| **Corresponding Author's Institution:** | Institut für Mineralogie |
| **Corresponding Author's Secondary Institution:** | |
| **First Author:** | Stephen Centrella |
| **First Author Secondary Information:** | |
| **Order of Authors:** | Stephen Centrella |
| | Andrew Putnis |
| | Pierre Lanari |
| | Håkon Austrheim |
| **Order of Authors Secondary Information:** | |
| **Funding Information:** | EU Initial Training Network “Flowtrans” (No. 316889) — Ph.D Stephen Centrella |
| | Australian Research Council (DP160103449) — Prof. Andrew Putnis |
| **Abstract:** | Centimetre-sized grains of Al-rich clinopyroxene within the granulitic anorthosites of the Bergen Arcs, W-Norway undergo deformation by faults and micro-shear zones (kinks) along which fluid has been introduced. The clinopyroxene (11 wt.% Al2O3) reacts to the deformation and hydration in two different ways: reaction to garnet (Alm43Prp32Grs24) plus a less aluminous pyroxene (3 wt.% Al2O3) along kinks and the replacement of the Al-rich clinopyroxene by chlorite along cleavage planes. We use electron probe microanalysis (EPMA) and mapping together with electron backscatter diffraction (EBSD) mapping to investigate the spatial and possible temporal relationships between these two paragenesis. Gresens' analysis has been used to determine the mass balance and the local volume changes associated with the two reactions. The reaction to garnet + low-Al clinopyroxene induces a loss in volume whereas the chlorite formation gains volume. Variations in the strain result in local variation in undulose extinction in the parent clinopyroxene. The specific mass evolution associated with both reactions suggests that they are associated with a single hydration event. EBSD results suggest that the density-increasing reaction to garnet + low-Al clinopyroxene takes place where the strain is highest whereas the density-decreasing reaction to chlorite forms away from shear zones where EBSD shows no significant strain. Pseudosection calculations suggest that the thermodynamic pressure of the assemblage within the shear zones is 15 kbar higher than the pressure conditions for the whole rock for the same range of temperature (~560°C). This result suggests that the deviatoric stress may play a role in determining the reactions that take place during retrograde metamorphism. |

# Textural and chemical evolution of pyroxene during hydration and deformation: a consequence of retrograde metamorphism.

Stephen Centrella[a,*], Andrew Putnis[a, b], Pierre Lanari[c], Håkon Austrheim[d]

[a] Institut für Mineralogie, University of Münster, D-48149 Münster, Germany

[b] The Institute for Geoscience Research (TIGeR), Curtin University, Perth, 6102, Australia

[c] Institute of Geological Sciences, University of Bern, CH3012 Bern, Switzerland

[d] PGP, Department of Geosciences, University of Oslo, N-0316, Norway

* E-mail corresponding author: centrella.stephen@uni-muenster.de

* Tel corresponding author: +49 251 83-33470

## Introduction

The partial hydration of a dry granulite facies rock from the lower crust during orogenesis and retrograde metamorphism is a fundamental process of re-equilibration of a rock with an initially low permeability. Understanding the interaction between fluid infiltration, mineral reactions and deformation in such a context is an important goal and has been the subject of many studies related to the mechanism of fluid transport, the role of deformation in initiating and driving fluid flow and the close relationship between mineral reaction, strength of a rock and deformation mechanisms (Beach and Fyfe 1972; Fyfe et al. 1978; Boundy et al. 1992; Marsh et al. 2009; Svahnberg and Piazolo 2010; Wawrzenitz et al. 2012; Fukuda et al. 2012; Gratier et al. 2013; Svahnberg and Piazolo 2013; Wintsch and Yeh 2013; Mukai et al. 2014).

Metamorphic reactions associated with fluid infiltration and hydration influence rock strength by forming new, softer minerals or by reducing the grain size (FitzGerald and Stünitz 1993; Bresser et al. 2001; Ronde et al. 2004; Ronde et al. 2005; Holyoke and Tullis 2006; Pearce et al. 2011). Moreover, the fluid phase present during metamorphism (Carmichael 1969; Putnis and Austrheim 2010; Philipotts and Ague 2013) can sometimes determining

whether dislocation creep or dissolution-precipitation creep play a major role in the deformation mechanism (Karato 1988; Rutter et al. 1994; Heidelbach et al. 2000; Menegon et al. 2008; Mukai et al. 2014).

Hydration also involves a local density change that may generate a local stress, depending on how open the system is to mass transport (Wheeler 1987; Ague 1991, 1994; Jamtveit et al. 2000; Jamtveit et al. 2008; Jamtveit and Hammer 2012; Kelemen and Hirth 2012; Centrella et al. 2015, 2016). Local stress developed during chemical reactions has been interpreted in terms of grain-scale pressure differences (Moulas et al. 2013; Tajčmanová et al. 2014; Wheeler 2014; Tajčmanová 2015; Tajčmanová et al. 2015; Vrijmoed and Podladchikov 2015), which are directly related to the mechanical properties of the deforming rocks. Variation of mineral assemblages on a small scale has been attributed to such local pressure variations which differ as a function of the stress direction (Vrijmoed and Podladchikov 2015). This concept is controversial and earlier estimates suggested that the magnitude of pressure deviation from the lithostatic value is small and almost insignificant if rocks are assumed to be weak and the differential stress that controls natural deformation is low (Brace et al. 1970; Burov et al. 2001; Jolivet et al. 2003). More recently Schmalholz and Podladchikov (2013) have shown that low viscosity zones may develop significant over- or under-pressure despite their low effective shear stress. A comprehensive review of the arguments for and against the consequences of non-lithostatic pressure difference has been recently published (Tajčmanová et al. 2015).

Another model highlighting the importance of stress generation by hydration has been presented by Wheeler (2014). As a function of the pathways of the fluid and the consequent reactions between different minerals, the differential stresses may produce assemblages that would otherwise be interpreted as higher or lower pressure than the actual pressure. This model is also currently being been challenged and debated (Schmalholz and Podladchikov

2014; Fletcher 2015; Wheeler 2015, 2015b; Tajčmanová et al. 2015; Hobbs and Ord 2015). Whatever the ultimate explanation, local stress variations in mineral reaction products during hydration have been observed in a number of studies (Ostapenko 1976; Jamtveit et al. 2009; Okamoto et al. 2011; Malvoisin et al. 2012) but their implications are yet to be fully understood.

In this paper we document a further example where different chemical reactions take place within a single crystal undergoing hydration and deformation. Our study is based on a sample from an outcrop in the Bergen Arcs, western Norway, where eclogite and amphibolite-facies hydration events associated with the Caledonian Orogeny (420 Ma) transect older anorthositic granulite-facies rocks (930 Ma). The Bergen Arcs are well known for examples of partially hydrated lower-crustal granulite where the contact between the granulite and the hydrated eclogite and amphibolite can be very sharp (Austrheim 1987; Boundy et al. 1992; Centrella et al. 2015, 2016). These two hydrated facies are related to the formation of shear zones along which fluid has been carried and reacted with the granulite (Austrheim 1987). Pseudotachylites, associated with earthquakes, are common throughout the region and may be implicated in the first stages of reaction and fracturing that facilitate fluid infiltration (Austrheim and Boundy 1994; Lund and Austrheim 2003; Austrheim 2013). The Bergen Arcs represent an exceptional window into the lower crust to study the consequence of fluid infiltration coupled with stress generation and deformation.

In this paper we describe an example of a hydration interface on a hand-specimen scale between a relatively dry anorthositic granulite and an amphibolite facies overprint. Within the granulite an Al-rich clinopyroxene with a garnet corona has been fractured by a fault and partly hydrated. Within the Al-rich clinopyroxene crystal, a network of deformation bands is associated with a new generation of garnet and a low-Al clinopyroxene while other parts of the same crystal are replaced by chlorite along cleavage planes. We investigate the spatial and

possible temporal and relationships between these two parageneses. Textural and chemical analyses have been carried by scanning electron microscopy (SEM), electron microprobe analysis (EMPA) and electron backscatter diffraction (EBSD) within a single grain of clinopyroxene.

## Geological Setting

In the Bergen Arcs, W-Norway, anhydrous Precambrian granulites are intermingled with Caledonian eclogite and amphibolite-facies assemblages. The Caledonian metamorphism at ~430Ma is associated with shear zones and veins and about 90% of the granulite is hydrated (Andersen et al. 1991). The lack of re-equilibration in the remaining granulite has been attributed to its anhydrous nature (Austrheim 1987) or that the thermal pulses were too short-lived to allow re-equilibration (Camacho et al. 2005). The amphibolites are generally interpreted as having formed during uplift although it has been noted that the only difference in major element chemical composition between the eclogites and amphibolites is a higher volatile content (loss on ignition– LOI) in the latter. From U/Pb dating on zircon in eclogite and amphibolite, the ages cannot be distinguished (~428Ma) whereas using Rb/Sr multi-mineral isochron ages, the amphibolite facies seems to be younger (~414Ma) (Glodny et al. 2008). Boundy et al. (1992) show that the amphibolite-facies metamorphism occurs along brittle fractures where the fluid enters and reacts into the shear zone through the granulite. Andersen et al. (1991) estimated the amphibolite-facies conditions at 4-7 kbar and 575-675°C and Boundy et al. (1996) at 10-12 kbar and 650-690°C.

### Sample description

The granulite facies anorthosites of the Bergen Arcs contain, in addition to plagioclase, Al-rich clinopyroxenes, garnet, locally S-rich scapolite, orthopyroxene and spinel (pleonaste).

The rock has a granulitic foliation visible by the elongated shape of the clinopyroxene aggregates (Fig.1). Some of the pyroxene lenses are rimmed by garnet, presumed to be the garnet corona formed in the granulites through much of the Bergen Arcs. The garnet coronas have been extensively described and are formed by reaction between olivine and plagioclase during the granulite facies metamorphism (Griffin and Heier 1973; Austrheim and Griffin 1985).

The interface between the dark granulite and the light-coloured hydrated granulite is sharply defined by the colour change in the feldspar from lilac-brown to milky-white (Fig.1a). Mukai et al. (2014) have described the milky, turbid feldspar in a similar sample from this area as a breakdown of the intermediate composition plagioclase to a complex intergrowth of Na-rich and Ca-rich plagioclase domains and the presence of many inclusions. The turbidity in feldspars has long been associated with the presence of micropores and inclusions associated with replacement reactions (Walker et al. 1995; Parsons and Lee 2009). The hydration front is not deformed and the overall fabric of the rock is unchanged, although within the hydrated part there are numerous small fractures and deformation features. All of these features are related to the hydration event with the formation of lower-grade and hydrous phases such as epidote, chlorite, mica and amphibole. One fault cuts the entire hand specimen but is only located in the hydrated part, passing through a pyroxene lens and displacing it by several millimetres (Fig 1b). The area around this fracture is the focus of this paper.

## Methods

Thin sections were studied by optical microscopy, scanning electron microscopy (SEM: JEOL JSM 6610LV), and by electron probe microanalysis (EPMA: JEOL 8530F) for quantitative element mapping at the University of Münster. The standard microprobe

conditions were 15 nA and 20 keV for quantitative analysis and 50 nA and 15 keV for the element mapping. Standards used for quantitative measurement were jadeite (Na), kyanite (Al), sanidine (K), olivine (Mg), hypersthene (Si), diopside (Ca), rhodocrosite (Mn), rutile (Ti), fayalite (Fe), and chromite (Cr). The software XMapTools 2.2.1 (Lanari et al. 2014) was used to quantify electron microprobe X-ray maps and to calculate the composition of specified areas within maps to follow the evolution of the local composition. Electron backscatter diffraction analysis (EBSD) with EDS data were carried out at the John de Laeter Centre, Curtin University using a field emission TESCAN MIRA3 SEM. EBSD data were acquired using an Oxford Instruments AZtec EBSD and EDS system. Post-processing of EBSD data to produce various property maps and pole figures was done using Oxford Instruments Channel 5.11 software. Pole figures are reported as lower hemisphere, equal-area projections. In all EBSD maps, a 6 nearest-neighbour noise zero solution noise reduction has been applied.

## Results

### Optical microscopy and scanning electron microscopy (SEM)

A merged image of backscattered electron images of the lens of clinopyroxene associated with a garnet corona is shown in Figure 2 (AAD2, location in Fig. 1b). The clinopyroxene lens is polycrystalline and made up of grains approximately 6 mm in size. The fault drawn in Figure 1 is located on the left of Figure 2 and shows a displacement indicated by the white arrows. The clinopyroxene (Cpx) located between the two layers of garnet (Grt(I)) contains a network of new garnet grains along kinks (Grt(II), red lines in Fig. 2) and chlorite (Chl) along Cpx cleavages (inside the green areas in Fig. 2). Mineral abbreviations are after (Kretz 1983).

The new generation of Grt(II) forms within the kink-bands that form a sub-parallel network through the Cpx lens while Chl forms along cleavage planes of the Cpx at a steep

angle to the garnet-bearing fractures. The domains where Chl is present (in green) are always located in the core of the Cpx, never on the rim close to the Grt corona (Figs. 2, 3a). The optical extinction of the Cpx is undulose in every individual grain present in the lens. At the tip of the kink-bands containing the new generation of Grt(II), there is well-developed undulose extinction in the Cpx (between the two dashed lines in Fig. 3b). This dark area starts at the tip and continues along the kink band through the Cpx crystal. No Chl is present in this domain. The zone of well-developed undulose extinction is as wide as the kink itself (100-150 µm).

Within the domains that contain chlorite, local variation of the optical extinction in the Al-rich Cpx is imaged as white linear features, approximately 50µm wide (Fig. 4a,b,c), that are sub-parallel to each other and also to the kink-banding network. The angular difference in the extinction position relative to the Cpx matrix is around 5°. Along these linear domains Chl is conspicuously absent nor do they generally contain Grt(II). In parts of the crystal where Grt(II) forms within Chl-free linear domains, deformation is visible as a kink band shown by the curved displacement of the Cpx cleavages (Fig. 4d,e). The Grt(II) grains are irregular in shape and are distributed along these kink-bands. The main difference between the Fig. 4d and e is the amount of Grt(II) within the kink. Figure 4e represents the typical kink banding visible in Fig. 2 and 3. Within the Chl domain, some calcite and titanite are present and are always associated with Chl formation along the cleavage planes of the Cpx (Fig. 5).

**Electron Probe Microanalysis**

Grt(I) located in the corona around the Cpx does not have any inclusions and has a constant composition of $Alm_{33}Prp_{44}Grs_{18}$ (Table 1 analyses 72 and 73), similar to garnets described from this locality by Erambert and Austrheim (1993). The Cpx composition is also constant throughout most of the grains, including near the Chl lamellae as well as near the Grt corona (Table 1 analyses 558 and 561).

An unusual feature of this Cpx is the high Al content (11 wt.% $Al_2O_3$), referred to here as Al-rich Cpx. However, along the linear features shown in Fig.4 and close to the Grt(II), the clinopyroxene has a different composition. The equivalent quantitative $Al_2O_3$ maps from the same area show this more clearly (Figs. 6, 7). In every case the clinopyroxene along the linear domains and associated with Grt(II) has a lower Al and Na but higher Mg, Ca and Si composition. The Al composition of the Cpx evolves from 11wt.% to 8wt.% of $Al_2O_3$ in this central part (Fig. 6b). The small black spots within the linear feature (Fig. 6b) where the aluminium concentration decreases may be porosity but could also be a consequence of loss of small Grt(II) grains during polishing. The Cpx composition is only altered along the thin band next to the Grt(II). The compositional interface between the Al-rich Cpx and low-Al Cpx is mostly relatively sharp without any measurable diffusion profile. In some places, this boundary is more diffuse and shows a gradational change in $Al_2O_3$ although this could also be due to an inclined interface between the two Cpx compositions. When the kink and Grt(II) formation are further developed (Fig. 4d), the Cpx associated with the Grt(II) has an even lower Al-content with $Al_2O_3$ at 5wt.% (Fig. 6d). The Grt(II) located in the kink has an average composition of $Alm_{43}Prp_{32}Grs_{24}$ with no visible chemical zoning (Table 1 analyses 82). These Grt(II) grains are never in contact with the Al-rich Cpx matrix and the low-Al Cpx makes a type of mantle, perfectly surrounding the garnet crystals.

Figure 7 shows a phase map, a compositional map of $Al_2O_3$ (in wt.%) and a map of the diopside end-member fraction of the Cpx surrounding the Grt(II) of the same area as in Fig.4e. In comparison to the kink in the previous figure (Fig. 6d), the surrounding Cpx has lost even more Al and Na but gained more Mg, Ca and Si (Table 1 analyses 566, 576 and 577). No Chl is present in this central part except in one unique area located in the lower part of the figure (in blue in the middle of the kink in Fig. 7a). The Grt(II) located in the kink has the same composition as that described in Fig. 6c ($Alm_{43}Prp_{32}Grs_{24}$) with no visible chemical

zoning (Table 1 analyses 85 and 90) and is always mantled by the low-Al Cpx. In Fig. 7 there are also small linear features containing Grt(II) and low-Al Cpx at approximately right angles to the main kink but within the Chl-free zone that extends for ~200µm parallel to the kink. The composition of the Chl is also listed in Table 1.

Based on the nomenclature of Morimoto (1988) and the Al content of the structural formulae (Al>0.1), the Al-rich and the low-Al Cpx are both aluminian diopside. The diopside component is 20% higher in the low-Al Cpx (0.83) than in the Al-rich Cpx (0.6) (Fig. 7c). The quantitative aluminium map and diopside end-member map were obtained using the structural formulae functions provided with the software XMapTools 2.2.1.

At the tip of the kink shown in Fig. 3b, the amphibole pargasite (Prg) is also formed. This is confirmed by quantitative analysis (Table 1) and imaged in Fig.8. This amphibole is separated from the Al-rich Cpx by the low-Al Cpx on one side whereas on the other, it is directly in contact with the Grt(II). The Chl-free region beyond the tip of the kink where the extinction is undulose also contains small grains of pargasite (shown in the lower part of Fig. 8b as lines with a slightly higher Al content). This is more clearly seen in the EBSD maps shown below (Fig.11). Based on Leake (1978), this end-member of calcic-amphibole contains (Na+K)>0.5 in the A-sites and between 6.5 and 7.5 Si atoms per formula unit (Table 1). Moreover, the Al site content greater than 1 indicates that it is an alumina-pargasite. However the occurrence of pargasite is uncommon and has only been observed in this one case at the termination of a kink.

**Electron Backscatter Diffraction (EBSD)**

Crystallographic orientation/information of minerals has been collected with EBSD along the region parallel to the same part of the kink as shown in Figure 7. The EDS map for Al, shows that the low-Al Cpx located in the centre of the kink has a high density of grain

boundaries (Fig. 9a) and individual Cpx grains are smaller than 50 µm. For more visibility, we didn't overlie the EDS map with the band contrast even if the grain boundary is related to the band contrast. Band contrast measures the image quality of the captured Kikuchi pattern essentially averaging the intensity of the Kikuchi bands with respect to the overall intensity within the EBSD and therefore shows both low and high angle grain boundaries shown as red and white lines in the low-Al Cpx region in Fig.9a. The band contrast map transparently overlain with the texture map (Fig.9b) shows that the low-Al Cpx has a misorientation of up to 25° compared to a reference point in the Al-rich Cpx (white cross in Fig. 9b). The misorientation of each grain increases from the rim to the core of the structure (Fig. 9c). The pole figure of low-Al Cpx grain orientations (Fig 9d) suggests that the crystallographic preferred orientation (CPO) is inherited from the parent Al-rich Cpx. The Grt(II) grains along the kink show weak CPO (Fig. 9e).

Optical microscopy shows that the area in the kink surrounding the Grt(II)+low-Al Cpx has an undulose extinction. With a reference point in this domain, Fig. 10 shows that the Cpx around the fracture is misoriented by about 1° relative to the bulk of the pyroxene that contains the Chl.  The width of these deformation bands is related to the amount of Grt(II) + low-Al Cpx formed, increasing from ~100µm (Figs. 4d, 6c) to ~200µm (Figs 4e, 7, 9, 10).

The EBSD data located from around the tip of the kink is shown in Fig. 11. The grain size and misorientation of the low-Cpx grains is similar to the low-Al Cpx all along the kink (Fig. 11b). The region beyond the tip that shows strong undulose extinction in Fig 3b, has a misorientation up to 10° relative to the reference point (white cross in Fig.11b), increasing from the rim to the centre but relatively constant along its length (Fig. 11c). Pargasite at the end of the kink is composed of different elongated grains around 25 µm long and less than 10 µm in width. Fine trails of the pargasite, best seen in Fig 11a as grey lines, also form within

the misoriented Cpx region. The low-Al Cpx inherits the crystallographic information of the parent Al-rich Cpx (Fig 11d) and the Grt(II) grains show only weak CPO (Fig. 11e).

## Discussion

The hand specimen shown in Figure 1 is typical of the type of interface between the granulite protolith and the amphibolite overprint that can be found in many outcrops in the Bergen Arcs. The lenses of the Al-rich Cpx and Grt were formed under granulite-facies conditions of around 10kbar and 850°C (Austrheim and Griffin 1985) at ~ 930 Ma (Bingen et al., 2001) and were partially hydrated and deformed during the Caledonian continental collision at ~430 Ma (Glodny et al. 2008). The hydration to amphibolite facies is often associated with shear zones and/or fracturing. Amphibolite-facies metamorphism occurs along brittle fractures where the fluid infiltrates and reacts into the shear zone through the granulite (Boundy et al. 1992). As in our hand specimen, fractures induce fluid infiltration through the rock and this is most clearly seen as the colour change in the feldspar (Mukai et al. 2014). Within the Al-rich Cpx a network of kink banding is formed. The fracturing, kink banding and hydration reactions are all broadly associated with the amphibolitisation "event" and the sharp interface between the dry granulite and the hydrated amphibolite suggests a discrete event that was terminated in both time and space at this interface.

The deformation features within the Al-rich Cpx could be interpreted as the result of the adjacent fault (Fig. 2) as a consequence of the Cpx being sandwiched between two competent layers of garnet (Grt(I)). The network of kink banding that crosscuts different Cpx crystals shows that the major stress component is not crystallographically controlled in this case. The various types of deformation bands and their associated mineralogy can also be interpreted as an evolution determined either as a time sequence or as a result of contemporaneous stress variations within the crystal. Figure 4 suggests such an evolution, from:

(i) the misorientation along linear features within the Al-rich Cpx, where no Chl exists but a central spine along the linear domain is replaced by a Cpx lower in Al, to

(ii) the progressive formation of a recognisable kink where Grt(II)+low-Al Cpx are formed, and

(iii) the final stage where the Al-content of the Cpx is reduced even further as the amount of Grt(II) formed along the kink increases.

A notable observation is that the linear features in Fig 4a,b are parallel to the kink bands containing the Grt(II) suggesting a common origin of the stress. The local deformation along the kink bands is shown by the misorientation in the Al-rich Cpx in a 200µm wide domain on either side of the Grt(II)+low-Al Cpx growth zone (Fig. 10). The increasing width of the kink with the proportion of Grt(II) (from ~100µm in Fig 4d to ~200µm in Fig 4e) may suggest that the growth of Grt(II) locally changes the rheology of the Al-rich Cpx and that the reaction to Grt(II) + Al-poor Cpx is related to a local variation of strain.

Away from the deformed regions, the Cpx is dense with chlorite (~40%) forming along cleavage planes. The cleavages are visibly displaced where the Grt(II)+Al-poor Cpx is best developed, giving a sense of shear as shown in Fig.4e. This could indicate that the shear post-dated the formation of the chlorite, although it is also possible that the cleavage planes were deformed by the shear and the Chl formed subsequently. The measured displacement of the cleavages across the kink increases with the proportion of Grt(II), from ~34µm in Fig 4d to ~71µm in Fig 4e.

From the textural data alone, the temporal relationship between the formation of the Chl and the Grt(II)+low-Al Cpx is equivocal. One possible scenario is that the kinks described here represent healed fractures where fluid infiltration initiated the local reaction of Al-rich Cpx to Grt(II)+low-Al Cpx. The low-angle deformation zone around these fractures could

then be the result of dislocation climb and recovery forming a network of sub-grain boundaries. The reaction to form Chl could be a later fluid infiltration event with the reaction taking place along previously deformed cleavage planes. On the other hand, the apparent spatial distribution and progressive development of the Grt(II)+low-Al Cpx in regions of higher strain, and the absence of Chl in these regions is a significant observation and may indicate that the local stress regime was a controlling factor in the reactions.

**Mass balance calculations**

Mass balance calculations provide an important clue to understanding element transfer and mobility in fluid-induced reactions (Gresens 1967; Centrella et al. 2015, 2016). To determine how the mass evolves within any reaction volume, it is necessary to estimate the local density of this volume, including all the phases present. For the reaction from Al-rich Cpx to Grt(II) + low-Al Cpx the densities of each phase were determined from the linear combination of end-members, assuming ideal solid solution. Densities of each end-member were obtained from the database present in the website of Barthelmy: http://webmineral.com/.

For the Grt(II) the estimated density was calculated from the components 43% almandine, 32% pyrope, 26% grossular and 1% spessartine (Table 1). Using equation 1 below gives a density of Grt(II) of 3.92 g.cm$^{-3}$.

$$density\ Grt(II) = (density_{Alm} \times X_{Alm}) + (density_{Prp} \times X_{Prp}) + (density_{Grs} \times X_{Grs}) + (density_{Sps} \times X_{Sps}) \quad (1)$$

where $density_{Alm}$ =4.32, $density_{Prp}$ =3.56, $density_{Grs}$ =3.59 and $density_{Sps}$ =4.19

We estimate the density of Al-rich Cpx as 3.49 g.cm$^{-3}$, based on a linear combination between hedenbergite-acmite-jadeite-diopside and Ca-Tschermark end-members. The data for these 5 end-members are present in the program XMapTools (Lanari et al. 2014) for a Ca-Na

pyroxene equivalent to the same composition as the Al-rich Cpx described here. Chlorite has a density of 2.6 g.cm$^{-3}$ based on a linear combination of Mg-Fe amesite-clinochlore-daphnite and sudoite. Using this data, it is possible the construct a density map for all phases from quantitative microprobe maps. Fig. 12a represents the density map calculated from the compositional maps using the method described above and the program XMapTools. The original Al-rich Cpx and the new low-Al Cpx both have a high diopside end-member component (Fig. 7c) and so the density between these two Cpx phases does not change significantly. However the low-Al Cpx together with Grt(II) makes the core of the kink denser than the Al-rich Cpx matrix.

The average densities of three different domains around the kink are derived from Figure 12a and sketched in Fig.12b. Compared to the parent Al-rich Cpx the central part of the kink composed of Grt(II)+low-Al Cpx is denser by ~2.9% while the domain of Al-rich Cpx+Chl is less dense by ~5.7%. These density changes require a redistribution of elements within the Al-rich Cpx crystal and the observation that these reactions are related to the amphibolisation event suggests a redistribution through the fluid phase.

By coupling the density maps computed from microprobe chemical maps with the mass balance equation of Gresens (1967), it is possible to see locally (on a micron to millimetre scale) gains or losses of each element associated with a reaction. In a Gresens analysis it is necessary to determine the relationship between the compositional changes and the volume changes associated with any reaction, and hence the densities of the phases involved must also be known. Note that in a commonly-used simplification of Gresens analysis (Grant 1986, 2005) termed isocon analysis, gains and losses of elements are calculated on the assumption that at least one element is immobile or that volume is preserved. The Gresens equation allows the system to be open for all components to be mobile and determines gains and losses of each component relative to the unaltered mineral or rock as a function of the volume

change (volume factor) for the reaction. This then needs to be combined with either microstructural observations or other evidence of specific element transport to determine the most likely combination of volume change and mass transfer. Here we are interested in the volume changes for the reaction to Grt(II)+low-Al Cpx and for the reaction to form Chl, both compared to the parent Al-rich Cpx. The composition of the Al-rich Cpx, the Chl and the Grt(II)+low-Al Cpx with their respective densities are shown in Table 2. The bulk composition for the domains Grt(II)+low-Al Cpx and for the Chl were obtained by selecting polygonal surfaces and extracting the corresponding local bulk composition using XMapTools (Mészáros et al. 2016).

From the Gresens equation, composition-volume diagrams show the gains and losses of each component in a reaction as a function of the volume factor for the reaction (Gresens 1967). In an open system a wide range of possible balanced equations is possible, each associated with different element gains and losses and volume factors. These are shown as linear plots for several major elements in Fig.13a. The zero gain-loss line defines reactions where specific elements are immobile. For example, if Al was immobile for the reaction of Al-rich Cpx to Grt(II)+low-Al Cpx, the volume factor would be 0.94 and the reaction would involve a loss of $SiO_2$ and CaO to the fluid and gains in MgO and FeO. On the other hand if $SiO_2$ was immobile the volume factor would be 1.03 and the reaction would involve a loss of CaO and a net gain of the other plotted elements. This is equivalent to a range between a volume loss of 6% and a volume gain of 3%.

The equivalent plot for the replacement of the parent Al-rich Cpx by Chl can take place over a wide range of volume factors between 0.96 and 2.1 (Fig. 13a) depending on whether Al or Si are considered to be immobile respectively. This means that the formation of Chl induces either a volume loss of up to 4% or gains up to 110% in volume. The gains and losses in volume in Fig.13a are relative to the volume of 100g of parent Al-rich Cpx.

Fig. 13b represents the mass gains and losses of components for these two reactions compared to the parent Al-rich Cpx over the respective range of volume factors. For both reactions the mass gains and losses are consistent and behave in the same way compared to the parent Al-rich Cpx: FeO, $Al_2O_3$, $Cr_2O_3$, MnO, MgO and $K_2O$ are gained whereas $SiO_2$, CaO and $Na_2O$ are lost. The percentages represent the values of mass gained and lost compared to the parent Al-rich Cpx composition. The error bars represent the mass values gained or lost for the range of different volumes of reaction defined by the Gresens equation (see Fig. 13a). Both reactions, to Grt(II)+low-Al Cpx and to Chl, involve a mass loss of CaO up to 21% and 98% respectively. The first assemblage contains around 15 wt.% of CaO whereas Chl does not contain Ca (Table 2). During the replacement of Al-rich Cpx by Chl, Ca is released into the fluid allowing calcic phases such as calcite and titanite to be formed (Fig. 5). Their association with Chl in the cleavage planes suggests the coupling with the replacement of chlorite. The formation of calcite and titanite also indicates the presence of $CO_2$ within the infiltrating fluid (Markl and Piazolo 1999). Over all the major elements plotted in Fig 13b the mass transfer behaves in the same way for the two different reactions within the respective range of volume factor, suggesting that the two reactions are likely to be related to the same fluid-induced event.

Over most of the plausible element exchange scenarios the Chl-forming reaction involves a local increase in volume, whereas the increased density for the Grt(II)+low-Al Cpx reaction involves a decrease in volume. This in turn would generate local stress within the crystal possibly resulting in fracturing and opening the cleavage planes for further fluid infiltration and chlorite growth. Using thermodynamic arguments, Wheeler (1987) has suggested that the differential stress produced by hydration reactions can also contribute to deformation processes. Based on microstructures and calculated stresses, the local stress produced by reactions that consume fluid can be up to a few hundred MPa (Jamtveit et al. 2000; Jamtveit

et al. 2008; Jamtveit et al. 2009; Jamtveit and Hammer 2012; Kelemen and Hirth 2012; Wheeler 2014, 2015, 2015b). In this context, we suggest the possibility that the stress generated by the formation of Chl might be locally compensated by the formation of Grt(II)+low-Al Cpx and by the mass transfer through the fluid phase and that variations in local stress may play a role in determining the reactions that take place.

**Local stress variations**

The consequences of local volume changes due to fluid–mineral reactions are being actively explored in relation to potential offsets of metamorphic reactions due to the generation of local stresses dependent on specific fluid pathways (Wheeler 2014). As a function of the pathways of the fluid, the differential stresses may produce assemblages that would otherwise be interpreted as higher or lower pressure than the actual pressure. Although the details of the model are currently under discussion (Schmalholz et al. 2014; Fletcher 2015; Wheeler 2015; Hobbs and Ord 2015) there is increasing evidence that volume changes and the resultant grain-scale pressure variations may drive metamorphic reactions (Wintsch and Andrews 1988; Tajčmanová et al. 2014; Tajčmanová 2015).

The differential stresses in the Al-rich Cpx, demonstrated by the variations in strain in the EBSD maps, could be implicated in the reactions described here. The reaction of Al-rich Cpx to Grt(II)+low-Al Cpx is located in kinks related to a local variation of stress and strain and the reaction generates a local volume decrease i.e. a local compression. Chlorite does not form along the kinks containing Grt(II) where the compressional stresses are highest and the volume increase in forming chlorite suggests local dilatational areas. This could indicate that the distribution of fluid in the rock might be controlled by the local stress distribution. A similar conclusion was reached by Mukai et al. (2014) who described a garnet in an amphibolitised garnulite, where one side of the garnet was replaced by quartz+kyanite while the other side, along a fluid-rich pathway was being replaced by chlorite and amphibole.

The presence of the amphibole pargasite (Prg) at the tip of one kink band suggests the existence of dilation on one side of the kink (Fig.11) as well as dilatational fractures filled with Prg ahead of the tip of the kink. This is where fluid could accumulate and form the hydrous phase.

**Modelling of phase equilibria**

Irrespective of whether the reactions described above are contemporaneous or not, it is nevertheless instructive to consider under what conditions the Al-rich Cpx would react to form Grt(II)+low-Al Cpx. This also raises the issue of when such equilibrium calculations are appropriate. If the reactions to Grt(II)+low-Al Cpx and to Chl took place at different times, a conventional P,T estimation might indicate a P,T path for the rock. On the other hand, if the reactions were contemporaneous, can local equilibrium be assumed as argued by Vrijmoed and Podladchikov (2015) despite the fact that the system as a whole is undergoing hydration, retrograde reactions and is out of equilibrium (Jamtveit et al. 2016).

We therefore use standard thermodynamic modelling to estimate the thermodynamic pressure and the temperature of formation for the specific assemblage. The standard state properties and solid solution models used for such semi-empirical calculations are based on experimental data made in an isotropic environment and as discussed above, it is likely that the stress distributions affect the mineral reactions in our system. Nevertheless, it may be instructive to determine the equilibrium P,T conditions for the garnet-forming reaction and compare this to the amphibolite facies P,T conditions. To determine this, we used the software Theriak-Domino (Capitani and Petrakakis 2010) with the thermodynamic database tc55 (Holland, T. J. B. and Powell 1998a) and subsequent updates (Mahar et al. 1997; White et al. 2000; White et al. 2002; Coggon and Holland. 2002; Holland and Powell 2003; Kelsey et al. 2005; Diener et al. 2007; White et al. 2007; Baldwin et al. 2005). The equilibrium models are computed using the local bulk composition of the domain Grt(II)+low-Al Cpx. The

corresponding anhydrous isochemical equilibrium phase diagrams are presented in figure 14. In figure 14a, the relevant field for the anhydrous assemblage Grt-Cpx-Qtz-Hem is shown in light grey. Although Qtz (quartz) and Hem (hematite) are predicted to be stable in this field and have not been found in the Cpx, they represent less than 3% of the calculated assemblage and they are neglected in the following discussion. A small excess of oxygen (0.4mol.%) stabilizes hematite because the solid solution of Cpx does not take all of it up as $Fe^{3+}$ (Table 2). This excess has been estimated on the basis of the structural formulae of Cpx. Using the Grt(II) isopleths to constrain the P-T conditions ($Alm_{43}Prp_{32}Grs_{24}$), it appears that this assemblage is stable between 21 and 27kbar and between 520-550°C (red domain in Fig.14a).

Since the reactions took place in the part of the rock hydrated at amphibolite-facies conditions (Fig. 1) with the presence of hydrous phases such as amphiboles, epidotes and chlorite, we consider how the addition of water affects the stability field of the Grt+low-Al Cpx assemblage. Using the same local bulk composition with 5 mol.% of water, the P-T conditions for the field Grt-Cpx-Qtz-Hem change very significantly to higher temperature (>700°C) for the same range of pressure (Fig. 14b). Water is present as a free phase in this assemblage showing that saturation is reached but the Grt(II) isopleths do not correspond to those observed. As the pressure range has not changed by addition of water, a T-$X_{H2O}$ diagram was calculated for a constant pressure of 25kbar (Fig. 14c) to see how the concentration of water influences the stability field of the assemblage. This diagram shows that when water is introduced to the system, the assemblage will be stable at temperature range between 730 to 800°C over the whole range of water content between 0.01 to 5 mol.%. However Grt(II) isopleths do not correspond to those observed.

To investigate the effect of water activity, a P-$a_{H2O}$ plot has been calculated for T=535$^0$C (Fig 14d). This temperature was chosen based on the temperature found in Fig. 14a. For an activity between 0 and 0.17, the assemblage Grt+Cpx (+minor Qtz and Hem) is stable and

Grt(II) isopleths can be modelled giving a pressure of 23-24kbar. A low water activity may be suggested by the small amount of calcite present between grains of Cpx, suggesting the presence of $CO_2$ in the fluid phase.

The thermodynamic model suggests that the assemblage located in the middle of the kink where the strain is high is stable at a low water activity (0 to 0.17) at a pressure around 24kbar and a temperature around 535°C. This temperature is in agreement with the temperature estimated for the whole rock of around 550-620°C (Fig. 15). However, for the whole rock composition the pressure estimation is completely different. The hydration shown in Figure 1 takes place at amphibolite facies conditions and the pseudosection for the whole rock composition gives a pressure estimate of between 9 and 11kbar using the albite isopleths ($Ab_{51}$) measured from feldspar in the matrix. The equilibrium pressure calculated for the reaction to Grt(II)+low-Al Cpx in the kink site is 15kbar higher.

We can now consider a number of possible interpretations of the textural and compositional data and the modelling:

1. The reaction of the Al-rich Cpx to Grt(II)+low-Al Cpx is not contemporaneous with the formation of Chl in the same crystal. The formation of Grt(II)+low-Al Cpx in kinks could represent healed fractures and deformation which predate the fluid event that formed the Chl. The high pressure stability for this reaction could then indicate an eclogite facies metamorphic event that is overprinted by an amphibolite metamorphism during subsequent uplift. The presence of an eclogite facies overprinting granulite has been well-documented in the Bergen Arcs (Austrheim 1987; Jamtveit et al. 1990; Bingen et al. 2004). However the superposition of two such events in the same hand specimen is difficult to reconcile with the lack of any evidence for an eclogite facies event elsewhere in the rock and the fact that the hydration event is defined spatially by the sharp

interface with the unreacted dry granulite suggesting a single event. The fact that the element losses and gains for the reaction to Grt(II)+low-Al Cpx and to Chl are similar also suggests a single hydration event.

2. The other alternative is that the reactions are broadly contemporaneous and associated with a single hydration event. This raises the immediate problem of how to interpret the 15kbar difference between the modelled reaction to Grt(II)+low-Al Cpx and the pressure calculated for the amphibolite facies whole rock. A pressure gradient of such magnitude in a single crystal does not seem feasible. However, such values are very similar to those predicted by Wheeler (2014) and by Tajčmanová et al. (2014) and Tajčmanová (2015). On the other hand, it may not be appropriate to use thermodynamic modelling for a hydration event that at least starts out far from equilibrium. However, arguments for local-scale equilibrium have been advanced by Evans et al. (2013) and Vrijmoed and Podladchikov (2015) even for situations where on a large scale the system is out of equilibrium, as discussed by Jamtveit et al. (2016).

On balance, we consider that the evidence presented here favours the second of these two interpretations, recognising that this challenges the classical view of metamorphic microstructures and the isograd concept.

## Conclusions

The textural evidence indicates that the reaction from Al-rich pyroxene to garnet + Al-poor pyroxene in some parts of the crystal and to chlorite in others is broadly contemporaneous. P-T estimates indicate a 15kbar difference between the reaction in the kink and that estimated for the whole rock. Whether such large pressure gradients are real or whether it is inappropriate to model phase equilibria in a non-equilibrium situation, where

local differences in the stress and availability of fluid may control reactions, is an open question.

Our conclusion takes the form of an hypothesis. In a rock or mineral where large stress gradients exist, retrograde hydration reactions taking place far from equilibrium may be influenced by factors other than the prevailing P,T conditions. We hypothesise that reactions may be driven by the tendency to reduce strain gradients by compensating positive volume changes in some areas by negative volume changes in other areas. Our observation that a volume reducing reaction from high-Al Cpx to Grt(II)+low-Al Cpx takes place in domains of high stress and strain around kinks banding while the volume increasing replacement of high-Al Cpx by chlorite takes place in regions of low stress and strain is broadly consistent with such an hypothesis. The reactions described here are induced by the overall hydration of the rock and it is likely that the redistribution of elements that will take place in a stress gradient is enhanced by mobility through a fluid phase.

**Acknowledgement**

This work is supported through the EU Initial Training Network “Flowtrans” Contract No. 316889 and by ARC Grant DP160103449 to AP. We thank Steve Reddy for help with collecting the EBSD data and the valuable comments and corrections suggested on an earlier version of the manuscript. We acknowledge helpful discussions with several colleagues including Bjørn Jamtveit and Olivier Galland

# References

Ague JJ (1991) Evidence for major mass transfer and volume strain during regional metamorphism of pelites. Geology 19:855–858

Ague JJ (1994) Mass transfer during Barrovian metamorphism of pelites, south– central Connecticut. 1. Evidence for changes in composition and volume. American Journal of Science 294:989–1057

Andersen T, Austrheim H, Burke E (1991) Fluid-induced retrogression of granulites in the Bergen Arcs, Caledonides of W. Norway: Fluid inclusion evidence from amphibolite-facies shear zones. Lithos 27(1):29–42. doi: 10.1016/0024-4937(91)90018-G

Austrheim H (1987) Eclogitization of lower crustal granulites by fluid migration through shear zones. Earth and Planetary Science Letters 81(2-3):221–232. doi: 10.1016/0012-821X(87)90158-0

Austrheim H (2013) Fluid and deformation induced metamorphic processes around Moho beneath continent collision zones: Examples from the exposed root zone of the Caledonian mountain belt, W-Norway. Tectonophysics 609:620–635. doi: 10.1016/j.tecto.2013.08.030

Austrheim H, Boundy M (1994) Pseudotachylytes Generated During Seismic Faulting and Eclogitization of the Deep Crust. Science 265

Austrheim H, Griffin WL (1985) Shear deformation and eclogite formation within granulite-facies anorthosites of the Bergen Arcs, western Norway. Chemical Geology 50(1-3):267–281. doi: 10.1016/0009-2541(85)90124-X

Baldwin JA, Powell R, Brown M, Moraes R, Fuck RA (2005) Modelling of mineral equilibria in ultrahigh-temperature metamorphic rocks from the Anápolis-Itauçu Complex, central Brazil. Journal of metamorphic Geology 23(7):511–531. doi: 10.1111/j.1525-1314.2005.00591.x

Barthelmy D Mineralogy Database, http://webmineral.com/

Beach A, Fyfe WS (1972) Fluid transport and shear zones at Scourie, Sutherland: evidence for overthrusting. Contr. Mineral. and Petrol. 36:175–180

Bingen B, Austrheim H, Whitehouse MJ, Davis WJ (2004) Trace element signature and U–Pb geochronology of eclogite-facies zircon, Bergen Arcs, Caledonides of W Norway. Contrib Mineral Petrol 147(6):671–683. doi: 10.1007/s00410-004-0585-z

Boundy TM, Essene EJ, Hall CM, Austrheim H, Halliday AN (1996) Rapid exhumation of lower crust during continent-continent collision and late extension: Evidence from 40Ar/39Ar incremental heating of hornblendes and muscovites, Caledonian orogen, western Norway. Geologic society of America 108(9):1425–1437

Boundy TM, Fountain DM, Austrheim H (1992) Structural development and petrofabrics of eclogite facies shear zones, Bergen Arcs, western Norway: implications for deep crustal deformational processes. Journal of metamorphic Geology 10:127–146

Brace WF, Ernst WG, Wittels Kallberg R (1970) An Experimental Study of Tectonic Overpressure in Franciscan Rocks. Geologic society of America 81:1325–1338

Bresser J de, Ter Heege J, Spiers C (2001) Grain size reduction by dynamic recrystallization: can it result in major rheological weakening? Int J Earth Sci 90(1):28–45. doi: 10.1007/s005310000149

Burov E, Jolivet L, Le Pourhiet L, Poliakov A (2001) A thermomechanical model of exhumation of high pressure (HP) and ultra-high pressure (UHP) metamorphic rocks in Alpine-type collision belts. Tectonophysics 342(1-2):113–136. doi: 10.1016/S0040-1951(01)00158-5

Camacho A, Lee, J. K W, Hensen BJ, Braun J (2005) Short-lived orogenic cycles and the eclogitization of cold crust by spasmodic hot fluids. Nature 435(7046):1191–1196. doi: 10.1038/nature03643

Capitani C de, Petrakakis K (2010) The computation of equilibrium assemblage diagrams with Theriak/Domino software. American Mineralogist 95(7):1006–1016. doi: 10.2138/am.2010.3354

Carmichael DM (1969) On the mechanism of prograde metamorphic reactions in quartz-bearing pelitic rocks. Contrib Mineral Petrol 20(20):244–267

Centrella S, Austrheim H, Putnis A (2015) Coupled mass transfer through a fluid phase and volume preservation during the hydration of granulite: An example from the Bergen Arcs, Norway. Lithos 236-237:245–255. doi: 10.1016/j.lithos.2015.09.010

Centrella S, Austrheim H, Putnis A (2016) Mass transfer and trace element redistribution during hydration of granulites in the Bergen Arcs, Norway. Lithos 262:1–10. doi: 10.1016/j.lithos.2016.06.019

Coggon R, Holland, T. J. B. (2002) Mixing properties of phengitic micas and revised garnet-phengite thermobarometers. J Metamorph Geol 20(7):683–696. doi: 10.1046/j.1525-1314.2002.00395.x

Diener JFA, Powell R, White RW, Holland, T. J. B. (2007) A new thermodynamic model for clino- and orthoamphiboles in the system Na2O-CaO-FeO-MgO-Al2O3-SiO2-H2O-O. J Metamorph Geol 25(6):631–656. doi: 10.1111/j.1525-1314.2007.00720.x

Erambert M, Austrheim H (1993) The effect of fluid and deformation on zoning and inclusion patterns in poly-metamorphic garnets. Contr. Mineral. and Petrol. 115(2):204–214. doi: 10.1007/BF00321220

Evans KA, Powell R, Frost BR (2013) Using equilibrium thermodynamics in the study of metasomatic alteration, illustrated by an application to serpentinites. Lithos 168-169:67–84. doi: 10.1016/j.lithos.2013.01.016

Fitz Gerald, J. D., Stünitz H (1993) Deformation of granitoids at low metamorphic grade. I: Reactions and grain size reduction. Tectonophysics(221):269–297

Fletcher CR (2015) Dramatic effects of stress on metamorphic reactions. Geology 255:e354. doi: 10.1130/G36302C.1

Fukuda JI, Okudaira T, Satsukawa T, Michibayashi K (2012) Solution–precipitation of K-feldspar in deformed granitoids and its relationship to the distribution of water. Tectonophysics 532-535:175–185. doi: 10.1016/j.tecto.2012.01.033

Fyfe WS, Price NJ, Thompson AB (1978) Fluids in the earth's crust. Elsevier, Amsterdam:383

Glodny J, Kühn A, Austrheim H (2008) Geochronology of fluid-induced eclogite and amphibolite facies metamorphic reactions in a subduction–collision system, Bergen Arcs, Norway. Contrib Mineral Petrol 156(1):27–48. doi: 10.1007/s00410-007-0272-y

Grant JA (1986) The Isocon Diagram--A Simple Solution to Gresens' Equation for Metasomatic Alteration. Economic Geology 81:1976–1982

Grant JA (2005) Isocon analysis: A brief review of the method and applications. Physics and Chemistry of the Earth, Parts A/B/C 30(17-18):997–1004. doi: 10.1016/j.pce.2004.11.003

Gratier JP, Dysthe D, Renard F (2013) The role of pressure solution creep in the ductility of the earth's upper crust. Archives Ouvertes:1–112

Gresens RL (1967) Composition-volume relationships of metasomatism. Chemical Geology 2:47–65. doi: 10.1016/0009-2541(67)90004-6

Griffin WL, Heier KS (1973) Petrological implications of some corona structures. Lithos 6(4):315–335. doi: 10.1016/0024-4937(73)90051-0

Heidelbach F, Post A, Tullis J (2000) Crystallographic preferred orientation in albite samples deformed experimentally by dislocation and solution precipitation creep. Journal of Structural Geology 22(11-12):1649–1661. doi: 10.1016/S0191-8141(00)00072-9

Hobbs B, Ord A (2015) Dramatic effects of stress on metamorphic reactions: COMMENT. Geology 43(11):e372. doi: 10.1130/G37070C.1

Holland T, Powell R (2003) Activity-Composition relations for phases in petrological calculations: an asymmetric multicomponent formulation. Contributions to Mineralogy and Petrology 145(4):492–501. doi: 10.1007/s00410-003-0464-z

Holland, T. J. B., Powell R (1990) An enlarged and updated internally consistent thermodynamic dataset with uncertainties and correlations: the system K2O–Na2O–CaO–MgO–MnO–FeO–Fe2O3–Al2O3–TiO2–SiO2–C–H2–O2. Journal of metamorphic Geology 8:89–124

Holland, T. J. B., Powell R (1998a) An internally consistent thermodynamic data set for phases of petrological interest. Journal of metamorphic Geology 16:309–343

Holland, T. J. B., Powell R (1998b) An internally consistent thermodynamic data set for phases of petrological interest. Journal of metamorphic Geology 16:309–343

Holland, T. J. B., Powell R (2006) Mineral activity?composition relations and petrological calculations involving cation equipartition in multisite minerals: a logical inconsistency. Journal of metamorphic Geology 24:851–861. doi: 10.1111/j.1525-1314.2006.00672.x

Holyoke CW, Tullis J (2006) The interaction between reaction and deformation: an experimental study using a biotite + plagioclase + quartz gneiss. Journal of metamorphic Geology 24(8):743–762. doi: 10.1111/j.1525-1314.2006.00666.x

Jamtveit B, Austrheim H, Malthe-Sørenssen A (2000) Accelerated hydration of the Earth's deep crust induced by stress perturbations. Nature 408:75–78

Jamtveit B, Austrheim H, Putnis A (2016) Disequilibrium metamorphism of stressed lithosphere. Earth-Science Reviews 154:1–13. doi: 10.1016/j.earscirev.2015.12.002

Jamtveit B, Bucher-Nurminen K, Austrheim H (1990) Fluid controlled eclogitization of granulites in deep crustal shear zones, Bergen arcs, Western Norway. Contrib Mineral Petrol 104

Jamtveit B, Hammer Ø (2012) Sculpting of Rocks by Reactive Fluids. Geochem Persp 1(3):341–481. doi: 10.7185/geochempersp.1.3

Jamtveit B, Malthe-Sørenssen A, Kostenko O (2008) Reaction enhanced permeability during retrogressive metamorphism. Earth and Planetary Science Letters 267(3-4):620–627. doi: 10.1016/j.epsl.2007.12.016

Jamtveit B, Putnis CV, Malthe-Sørenssen A (2009) Reaction induced fracturing during replacement processes. Contrib Mineral Petrol 157(1):127–133. doi: 10.1007/s00410-008-0324-y

Jolivet L, Faccenna C, Goffé B, Burov E, Agard P (2003) Subduction tectonics and exhumation of high-pressure metamorphic rocks in the Mediterranean Orogens. American Journal of Science 303:353–409

Karato SI (1988) The role of recrystallization in the preferred orientation of olivine. Physics of the Earth and Planetary Interiors 51(1-3):107–122. doi: 10.1016/0031-9201(88)90029-5

Kelemen PB, Hirth G (2012) Reaction-driven cracking during retrograde metamorphism: Olivine hydration and carbonation. Earth and Planetary Science Letters 345-348:81–89. doi: 10.1016/j.epsl.2012.06.018

Kelsey DE, White RW, Powell R (2005) Calculated phase equilibria in K2O-FeO-MgO-Al2O3-SiO2-H2O for silica-undersaturated sapphirine-bearing mineral assemblages. J. Metamorph Geol (Journal of Metamorphic Geology) 23(4):217–239. doi: 10.1111/j.1525-1314.2005.00573.x

Kretz R (1983) Symbols for rock-forming minerals. American Mineralogist 68:277–279

Lanari P, Vidal O, Andrade V, Dubacq B, Lewin E, Grosch EG, Schwartz S (2014) XMapTools: A MATLAB©-based program for electron microprobe X-ray image processing and geothermobarometry. Computers & Geosciences 62:227–240. doi: 10.1016/j.cageo.2013.08.010

Leake BE (1978) Nomenclature of amphiboles. American Mineralogist:1023–1052

Lund MG, Austrheim H (2003) High-pressure metamorphism and deep-crustal seismicity: evidence from contemporaneous formation of pseudotachylytes and eclogite facies coronas. Tectonophysics 372(1-2):59–83. doi: 10.1016/S0040-1951(03)00232-4

Mahar EM, Baker JM, Powell R, Holland, T. J. B., Howell N (1997) The effect of Mn on mineral stability in metapelites. J Metamorph Geol 15(2):223–238. doi: 10.1111/j.1525-1314.1997.00011.x

Malvoisin B, Brunet F, Carlut J, Rouméjon S, Cannat M (2012) Serpentinization of oceanic peridotites: 2. Kinetics and processes of San Carlos olivine hydrothermal alteration. J. Geophys. Res. 117(B04102). doi: 10.1029/2011JB008842

Markl G, Piazolo S (1999) Stability of high-Al titanite from low-pressure calcsilicates in light of fluid and host-rock composition. American Mineralogist 84(1-2):37–47. doi: 10.2138/am-1999-1-204

Marsh JH, Johnson SE, Yates MG, West, T JR, D. P. (2009) Coupling of deformation and reactions during mid-crustal shear zone development: an in situ frictional-viscous transition. Journal of metamorphic Geology 27(8):531–553. doi: 10.1111/j.1525-1314.2009.00841.x

Menegon L, Pennacchioni G, Spiess R (2008) Dissolution-precipitation creep of K-feldspar in mid-crustal granite mylonites. Journal of Structural Geology 30(5):565–579. doi: 10.1016/j.jsg.2008.02.001

Mészáros M, Hofmann BA, Lanari P, Korotev RL, Gnos E, Greber ND, Leya I, Greenwood RC, Jull AJT, Al-Wagdani K, Mahjoub A, Al-Solami AA, Habibullah SN (2016) Petrology and geochemistry of feldspathic impact-melt breccia Abar al' Uj 012, the first lunar meteorite from Saudi Arabia. Meteorit Planet Sci:1–19. doi: 10.1111/maps.12693

Morimoto N (1988) Nomenclature of pyroxenes. American Mineralogist 73:1123–1133

Moulas E, Podladchikov YY, Aranovich LY, Kostopoulos D (2013) The problem of depth in geology: When pressure does not translate into depth. Petrology 21(6):527–538. doi: 10.1134/S0869591113060052

Mukai H, Austrheim H, Putnis CV, Putnis A (2014) Textural Evolution of Plagioclase Feldspar across a Shear Zone: Implications for Deformation Mechanism and Rock Strength. Journal of Petrology 55(8):1457–1477. doi: 10.1093/petrology/egu030

Okamoto A, Ogasawara Y, Ogawa Y, Tsuchiya N (2011) Progress of hydration reactions in olivine–H2O and orthopyroxenite–H2O systems at 250°C and vapor-saturated pressure. Chemical Geology 289:245–255. doi: 10.1016/j.chemgeo.2011.08.007

Ostapenko GT (1976) Excess pressure on the solid phases generated by hydration (according to experimental data on the hydration of periclase). Geokhimikiya 6:824–844

Parsons I, Lee MR (2009) Mutual replacement reactions in alkali feldspars I: microtextures and mechanisms. Contrib Mineral Petrol 157(5):641–661. doi: 10.1007/s00410-008-0355-4

Pearce MA, Wheeler J, Prior DJ (2011) Relative strength of mafic and felsic rocks during amphibolite facies metamorphism and deformation. Journal of Structural Geology 33(4):662–675. doi: 10.1016/j.jsg.2011.01.002

Philipotts A, Ague J (2013) Principles of Igneous and Metamorphic Petrology, Cambridge University

Putnis A, Austrheim H (2010) Fluid-induced processes: metasomatism and metamorphism. Geofluids. doi: 10.1111/j.1468-8123.2010.00285.x

Ronde AA de, Heilbronner R, Stünitz H, Tullis J (2004) Spatial correlation of deformation and mineral reaction in experimentally deformed plagioclase–olivine aggregates. Tectonophysics 389(1-2):93–109. doi: 10.1016/j.tecto.2004.07.054

Ronde AA de, Stünitz H, Tullis J, Heilbronner R (2005) Reaction-induced weakening of plagioclase–olivine composites. Tectonophysics 409(1-4):85–106. doi: 10.1016/j.tecto.2005.08.008

Rutter EH, Casey M, Burlini L (1994) Preferred crystallographic orientation development during the plastic and superplastic flow of calcite rocks. Journal of Structural Geology 16(10):1431–1446. doi: 10.1016/0191-8141(94)90007-8

Schmalholz SM, Duretz T, Schenker FL, Podladchikov YY (2014) Kinematics and dynamics of tectonic nappes: 2-D numerical modelling and implications for high and ultra-high pressure tectonism in the Western Alps. Tectonophysics 631:160–175. doi: 10.1016/j.tecto.2014.05.018

Schmalholz SM, Podladchikov Y (2014) Metamorphism under stress: The problem of relating minerals to depth. Geology 42(8):733–734. doi: 10.1130/focus0822014.1

Schmalholz SM, Podladchikov YY (2013) Tectonic overpressure in weak crustal-scale shear zones and implications for the exhumation of high-pressure rocks. Geophys. Res. Lett. 40(10):1984–1988. doi: 10.1002/grl.50417

Svahnberg H, Piazolo S (2010) The initiation of strain localisation in plagioclase-rich rocks: Insights from detailed microstructural analyses. Journal of Structural Geology 32(10):1404–1416. doi: 10.1016/j.jsg.2010.06.011

Svahnberg H, Piazolo S (2013) Interaction of chemical and physical processes during deformation at fluid-present conditions: a case study from an anorthosite–leucogabbro deformed at amphibolite facies conditions. Contrib Mineral Petrol 165(3):543–562. doi: 10.1007/s00410-012-0822-9

Tajčmanová L (2015) Deviations from lithostatic pressure during metamorphism: fact or fiction? J. Metamorph. Geol. 33(8):783–784. doi: 10.1111/jmg.12152

Tajčmanová L, Podladchikov Y, Powell R, Moulas E, Vrijmoed JC, Connolly J (2014) Grain-scale pressure variations and chemical equilibrium in high-grade metamorphic rocks. J. Meta. Geol. 32(2):195–207. doi: 10.1111/jmg.12066

Tajčmanová L, Vrijmoed J, Moulas E (2015) Grain-scale pressure variations in metamorphic rocks: implications for the interpretation of petrographic observations. Lithos 216-217:338–351. doi: 10.1016/j.lithos.2015.01.006

Vrijmoed JC, Podladchikov YY (2015) Thermodynamic equilibrium at heterogeneous pressure. Contrib Mineral Petrol 170(1). doi: 10.1007/s00410-015-1156-1

Walker, F. D. L., Lee MR, Parsons I (1995) Micropores and micropermeable texture in alkali feldspars: geochemical and geophysical implications. Mineralogical Magazine 59:505–534

Wawrzenitz N, Krohe A, Rhede D, Romer RL (2012) Dating rock deformation with monazite: The impact of dissolution precipitation creep. Lithos 134-135:52–74. doi: 10.1016/j.lithos.2011.11.025

Wheeler J (2015b) Dramatic effects of stress on metamorphic reactions. Geology:373. doi: 10.1063/1.1702656

Wheeler J (1987) The significance of grain-scale stresses in the kinetics of metamorphism. Contrib Mineral Petrol 97:397–404

Wheeler J (2014) Dramatic effects of stress on metamorphic reactions. Geology 42(8):647–650. doi: 10.1130/G35718.1

Wheeler J (2015) Dramatic effects of stress on metamorphic reactions: COMMENT. Geology 43(1):e355. doi: 10.1130/G36302C.1

White RW, Powell R, Clarke GL (2002) The interpretation of reaction textures in Ferich metapelitic granulites of the Musgrave Block, central Australia: constraints from mineral equilibria calculations in the system K2OFeOMgOAl2O3SiO2H2OTiO2Fe2O3. J Metamorph Geol 20:41–55

White RW, Powell R, Holland, T. J. B. (2007) Progress relating to calculation of partial melting equilibria for metapelites. J Metamorph Geol 25(5):511–527. doi: 10.1111/j.1525-1314.2007.00711.x

White RW, Powell R, Holland, T. J. B., Worley BA (2000) The effect of TiO2 and Fe2O3 on metapelitic assemblages at greenschist and amphibolite facies conditions: mineral equilibria calculations in the system K2O-FeO-MgO-Al2O3-SiO2-H2O-TiO2-Fe2O3. J Metamorph Geol 18:497–511

Wintsch RP, Andrews MS (1988) Deformation Induced Growth of Sillimanite: "Stress" Minerals Revisited. Chicago Journals 96(2):143–161

Wintsch RP, Yeh MW (2013) Oscillating brittle and viscous behavior through the earthquake cycle in the Red River Shear Zone: Monitoring flips between reaction and textural softening and hardening. Tectonophysics 587:46–62. doi: 10.1016/j.tecto.2012.09.019

Table captions:

**Table 1:** Microprobe analyses of garnet, clinopyroxene and chlorite. Each structural formula has been calculated using the software AX of Holland, and Powell (2006). Estimation of the ferric iron ($Fe^{3+}$) was made following the calculation described in Holland and Powell (1990, 1998b)

**Table 2:** Table representing the local bulk composition of the Al-rich Cpx, Grt(II)+low-Al Cpx and Chl with respective densities.

Figure captions:

**Fig. 1**: Photograph of the hand sample of (a) the granulite and (b) the interpretative sketch.

**Fig. 2:** SEM backscatter image of a part of the Cpx lens with representation of the chlorite-bearing domains (in green) and the new garnet generation (in red).

**Fig. 3**: a) Crossed polarized microscope image of the clinopyroxene lens surrounded by garnet with location of the main fault. b) Crossed polarized microscope image of the new generation of garnet (Grt(II)) along a fracture where the clinopyroxene at the tip shows strong undulose extinction (white arrow between dashed lines). Image b) is rotated 90° anticlockwise relative to the orientation in a).

**Fig. 4**: a) Crossed polarized microscope image of the undulose extinction in the Al-rich Cpx within the Chl domain and (b) its schematic sketch. c) Backscattered image localized in these undulose extinction regions. d) SEM Backscattered image localized in another undulose extinction domain where garnet and kink deformation start to form. e) SEM backscatter image with representation of a kink deformation and the associated deformation (dashed lines).

**Fig. 5:** SEM backscatter image showing where titanite (Ttn) is located within the Chl domain.

**Fig. 6:** a) Phase map presented in Fig. 4a, b, c and its associated quantitative microprobe map of $Al_2O_3$. c) Phase map presented in Fig. 4d and its associated quantitative microprobe map of $Al_2O_3$. The maps were obtained using the software XMapTools v. 2.1.1 from Lanari et al. (2014).

**Fig. 7**: a) Phase map located in the kink presented in Fig. 4e. b) Quantitative microprobe map of $Al_2O_3$ and c) Composition of the Cpx expressed as the diopside end-member concentration through the map. The maps were obtained using the software XMapTools v. 2.1.1 from Lanari et al. (2014).

**Fig. 8**: a) Backscatter SEM image of picture presented in Fig. 3b and (b) its associated quantitative microprobe map in $Al_2O_3$.

**Fig. 9**: EBSD data from Cpx. a) EDS map of Al. Red lines represent the grain boundary between 2 and 10° and white lines >10°. b) Texture map overlain with band contrast for Cpx. Step size of the maps was 1 µm. c) Misorientation profile of the white line drawn in (b). Reference crystal is represented by the white cross in (b). d) Lower hemisphere equal area projection showing the Cpx crystal orientations (524335 data points). Colors in the map b) and the pole figures d) are correlated. e) Lower hemisphere equal area projection showing crystal orientations (16495 data points) of the Grt(II) grains along the fracture.

**Fig. 10**: Texture map overlain with band contrast for Cpx. Step size of the maps was 1 µm. Reference crystal is represented by the white cross.

**Fig. 11**: EBSD data from Cpx at the tip of the new generation of Grt. a) Phase map overlain with band contrast. b) Texture map overlain with band contrast. Step size of the maps was 0.35 µm. c) Misorientation profile of the white line drawn in (b). Reference crystal is represented by the white cross in (a). d) Lower hemisphere equal area projection showing the Cpx crystal orientations (1376490 data points). Colors in the map b) and the pole figures d) are correlated. e) Lower hemisphere equal area projection showing the Grt crystal orientations (33686 data points).

**Fig. 12**: a) Density map obtained with XMapTools v. 2.2.1 (Lanari et al. 2014). b) Average densities for different domains: Al-rich Cpx (grey), Grt(II)+low-Al Cpx (orange) and Al-rich Cpx+Chl (blue).

**Fig. 13**: a) The overall gains and losses of elements from the replacement of Al-rich Cpx by Grt(II)+low-Al Cpx and Al-rich Cpx by Chl during the hydration of the granulite, calculated from quantitative microprobe maps coupled with the Gresens analysis. b) The overall gains and losses for

both reactions within the available range of volume factors. $TiO_2$, $Cr_2O_3$ and $K_2O$ are missing because their concentrations are below the detection limit of the microprobe.

**Fig. 14:** P-T pseudosections using the bulk composition of the assemblage Grt(II)+low-Al Cpx (a) without water and (b) with water in the system. For more visibility, the isopleths in (a) are not all represented. The assemblage field is represented in light grey and the peak condition in red using Grt isopleths. c) T-$X_{H2O}$ pseudosection in function of the water content in the system for 25kbar. d) P-X pseudosection in function of the activity of the water for 535°C

**Fig. 15**: P-T pseudosection for the bulk rock composition:
SI(48.94)AL(30.50)FE(0.65)MG(0.63)CA(10.83)NA(8.45)H(1)O(?)

Figure 1

Click here to download Figure Figure 1.tif

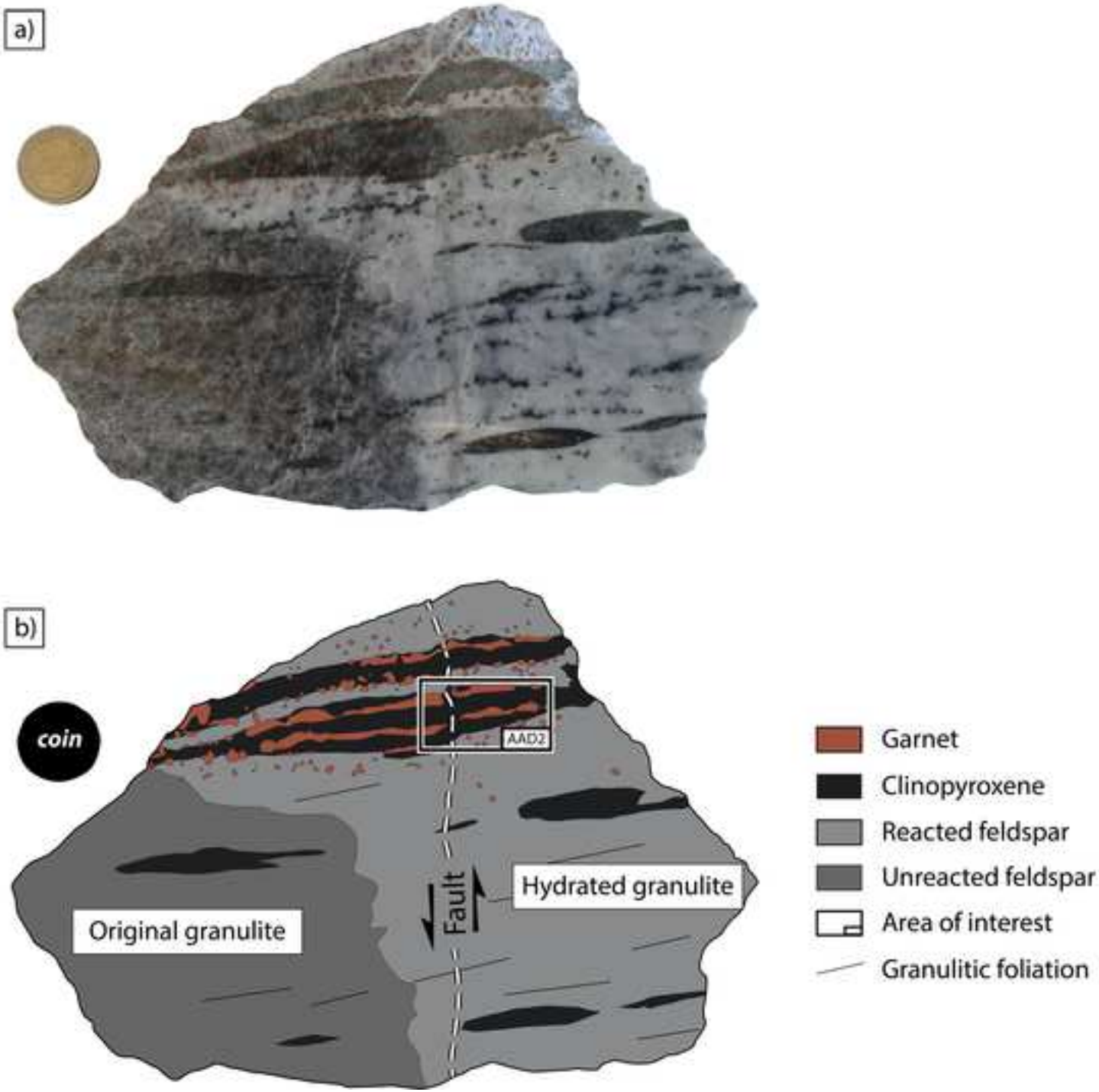

Figure 2

Click here to download Figure Figure 2.tif

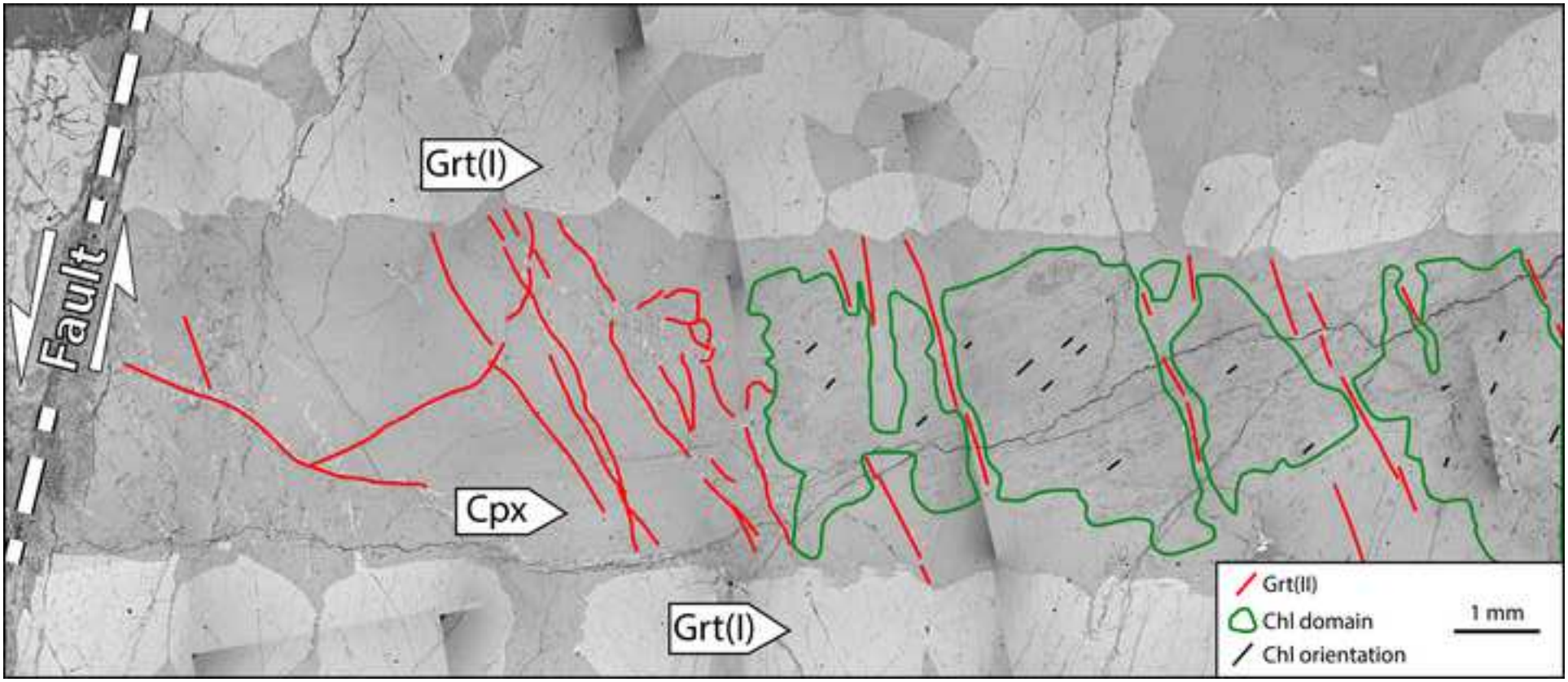

Figure 3

Click here to download Figure Figure 3.tif

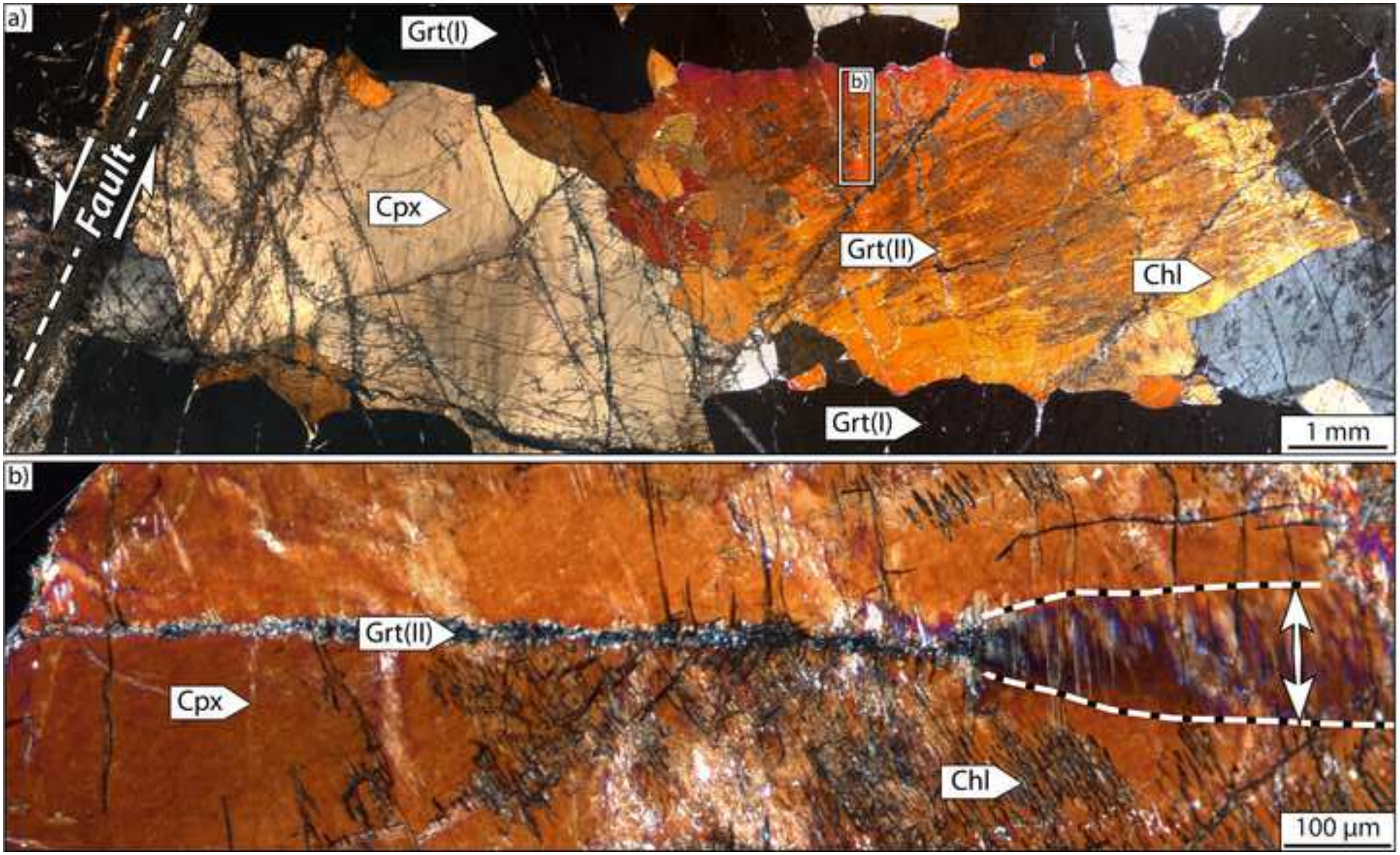

Figure 4

Click here to download Figure Figure 4.tif

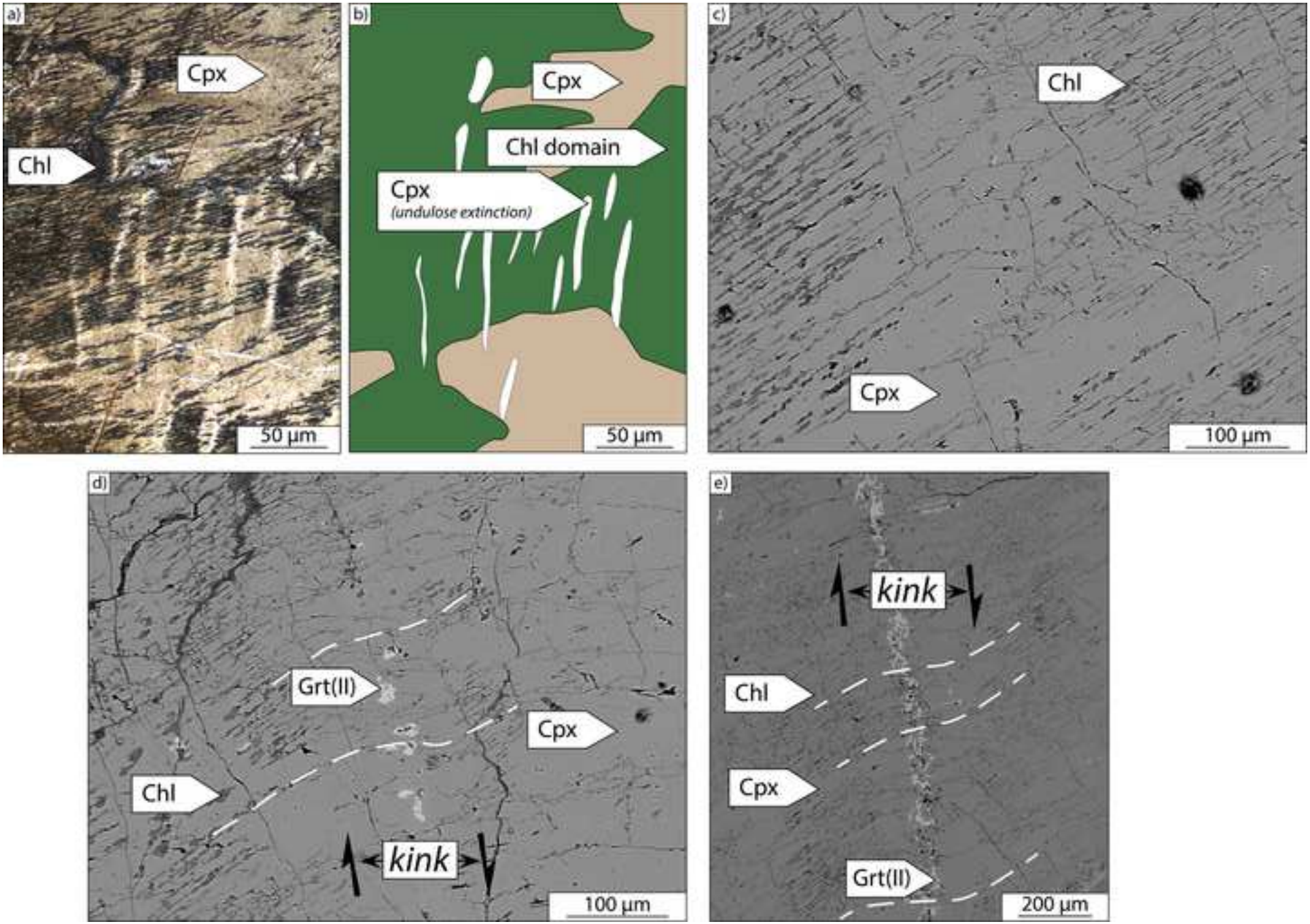

Figure 5

Click here to download Figure Figure 5.tif

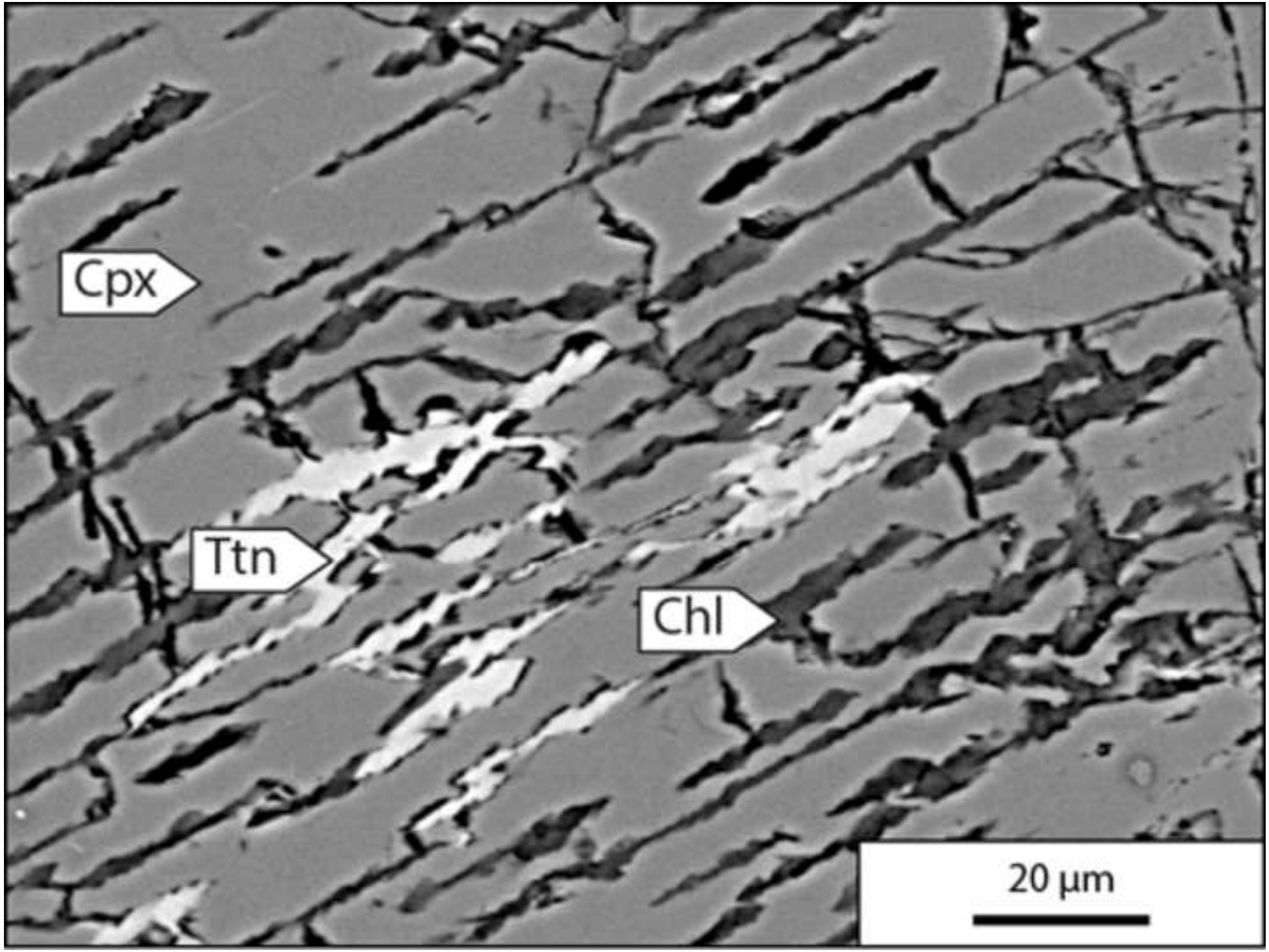

Figure 6

Click here to download Figure Figure 6.tif

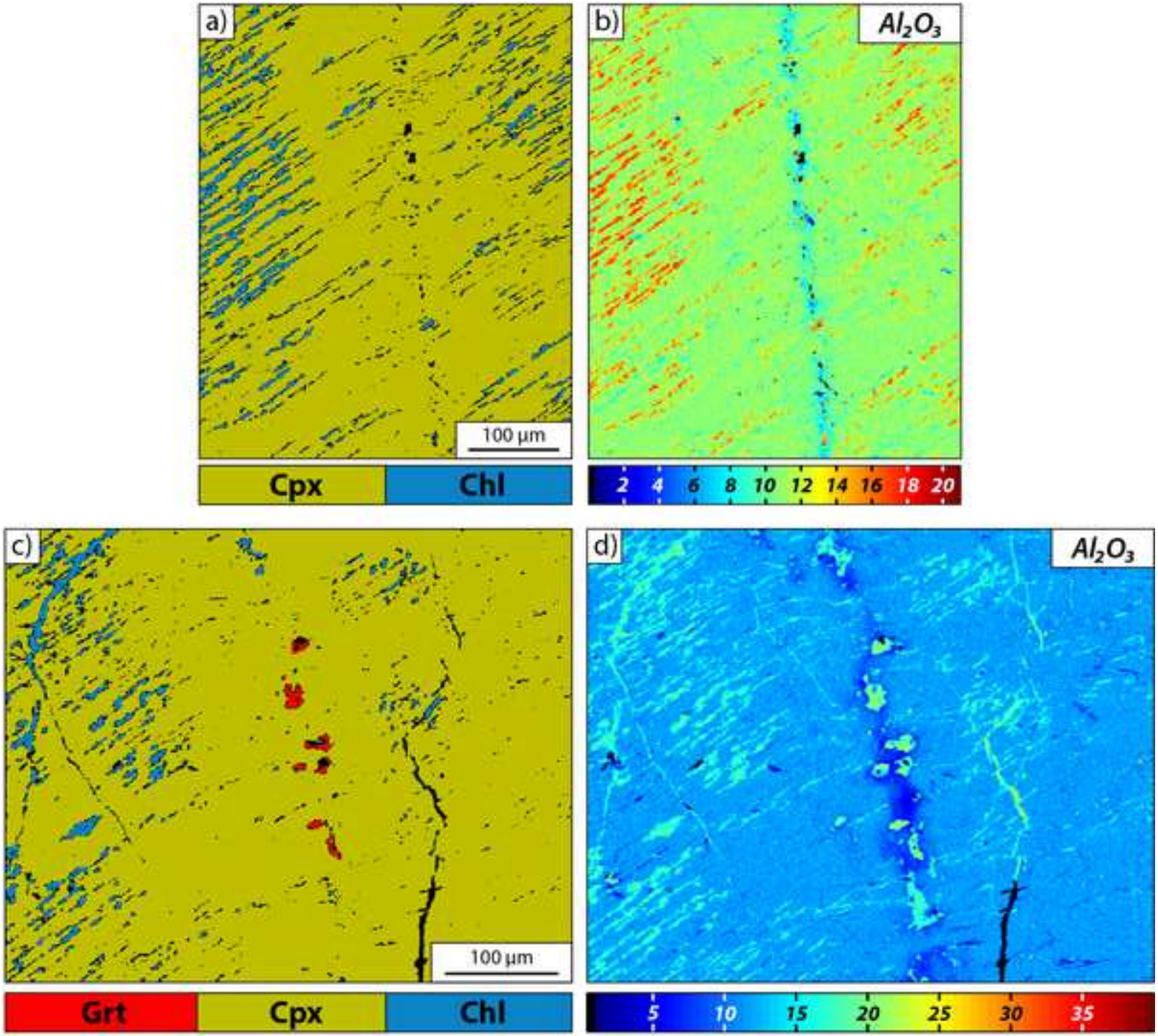

Figure 7

Click here to download Figure Figure 7.tif

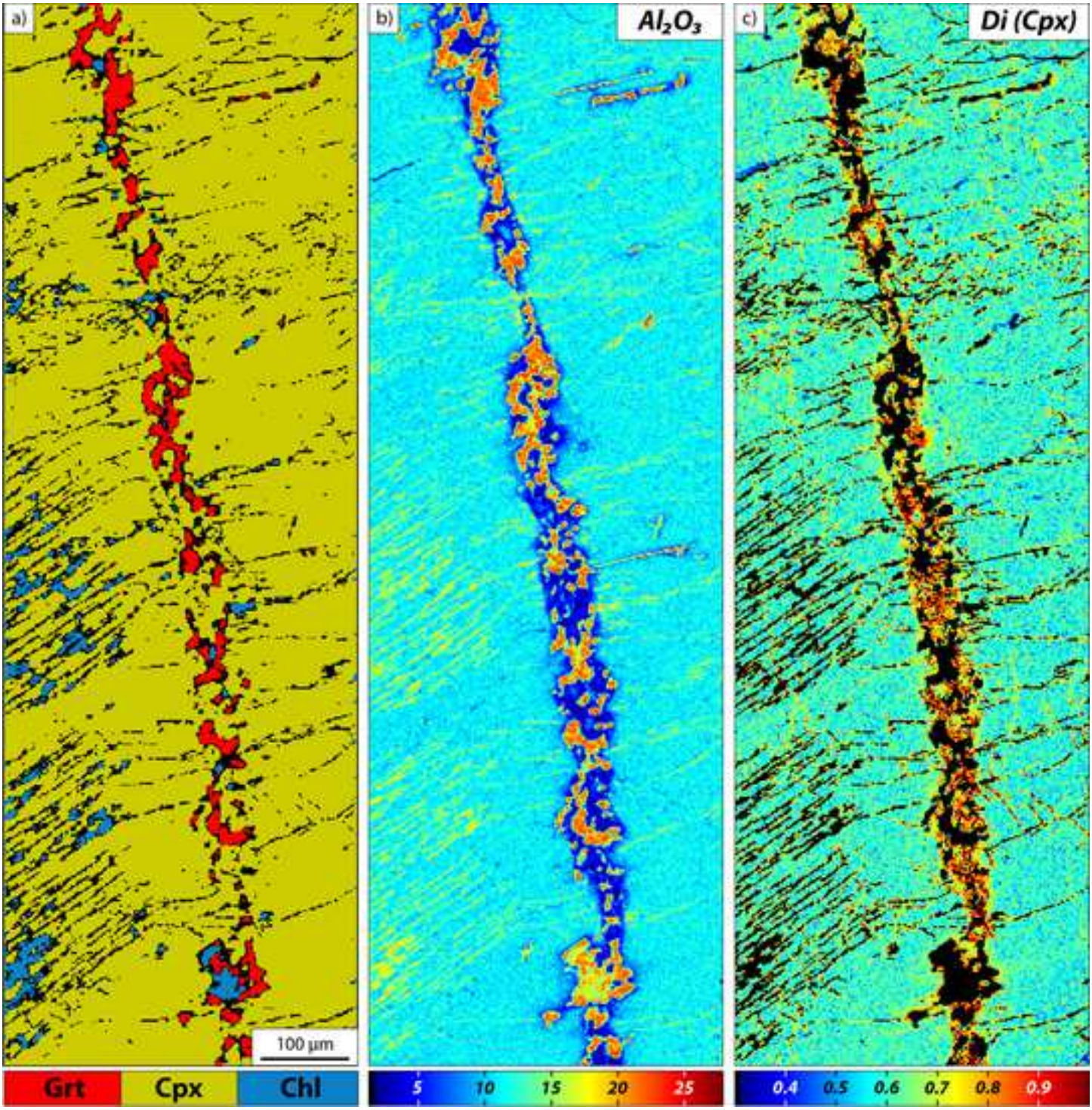

Figure 8

Click here to download Figure Figure 8.tif

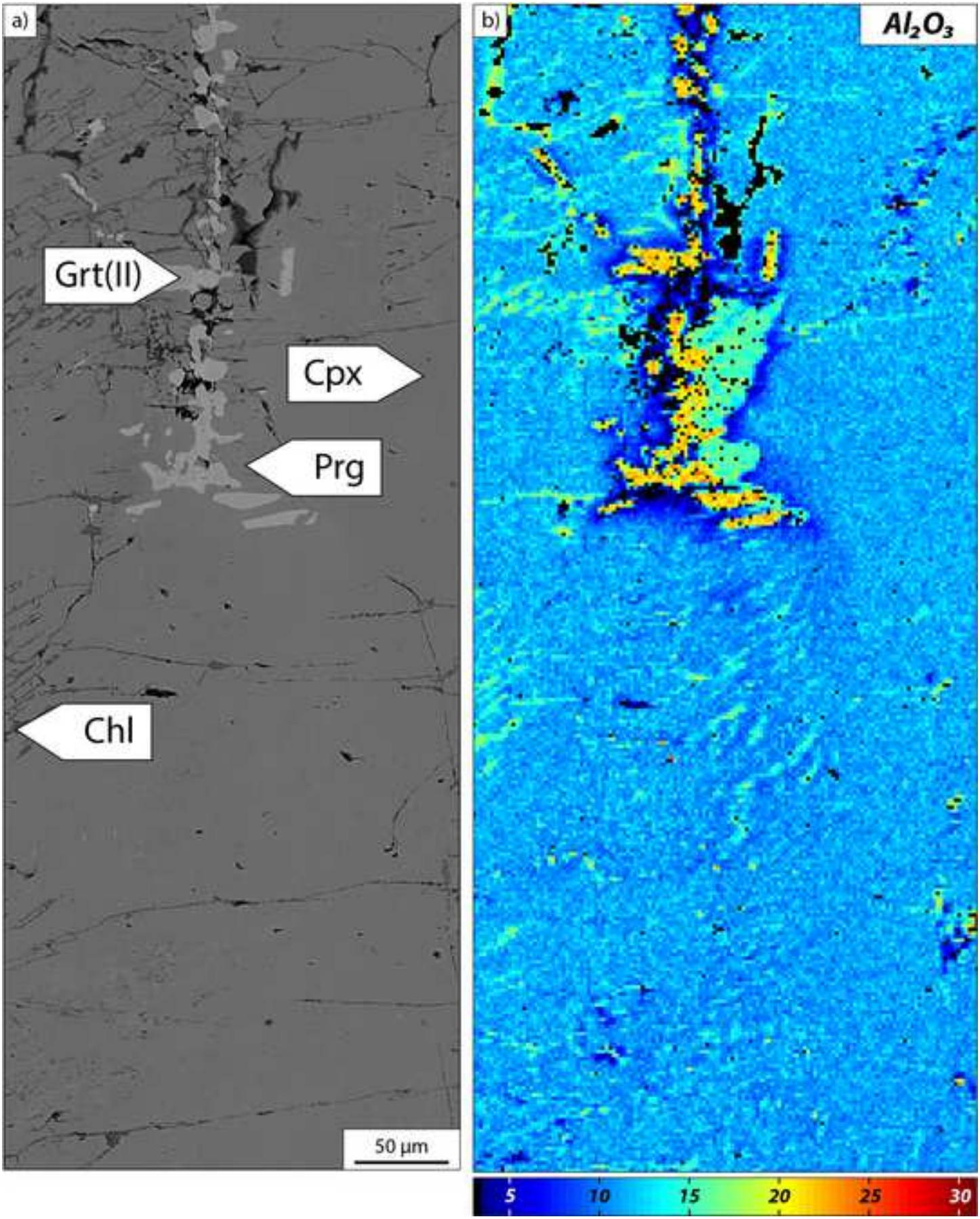

Figure 9

Click here to download Figure Figure 9.tif

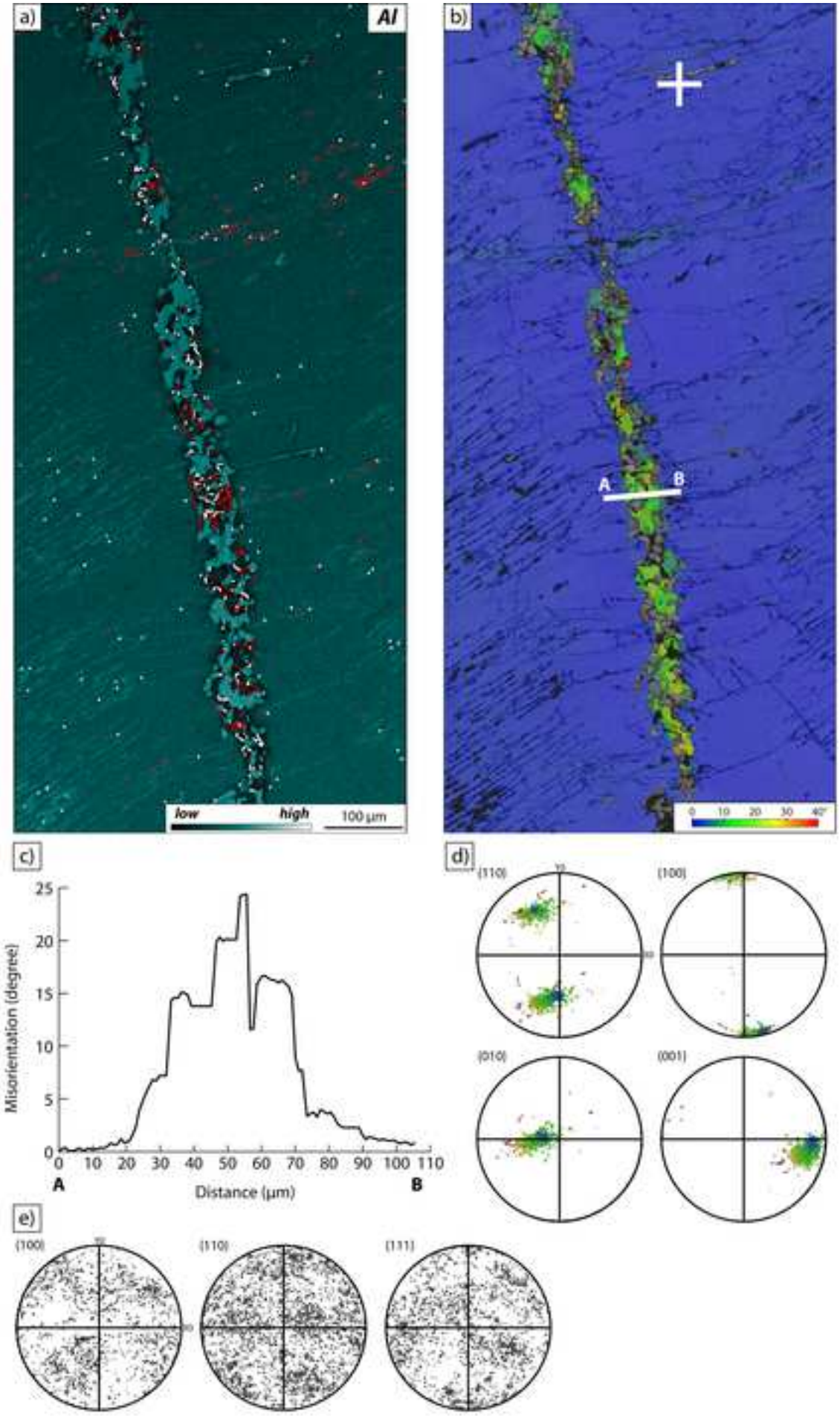

Figure 10

Click here to download Figure Figure 10.tif

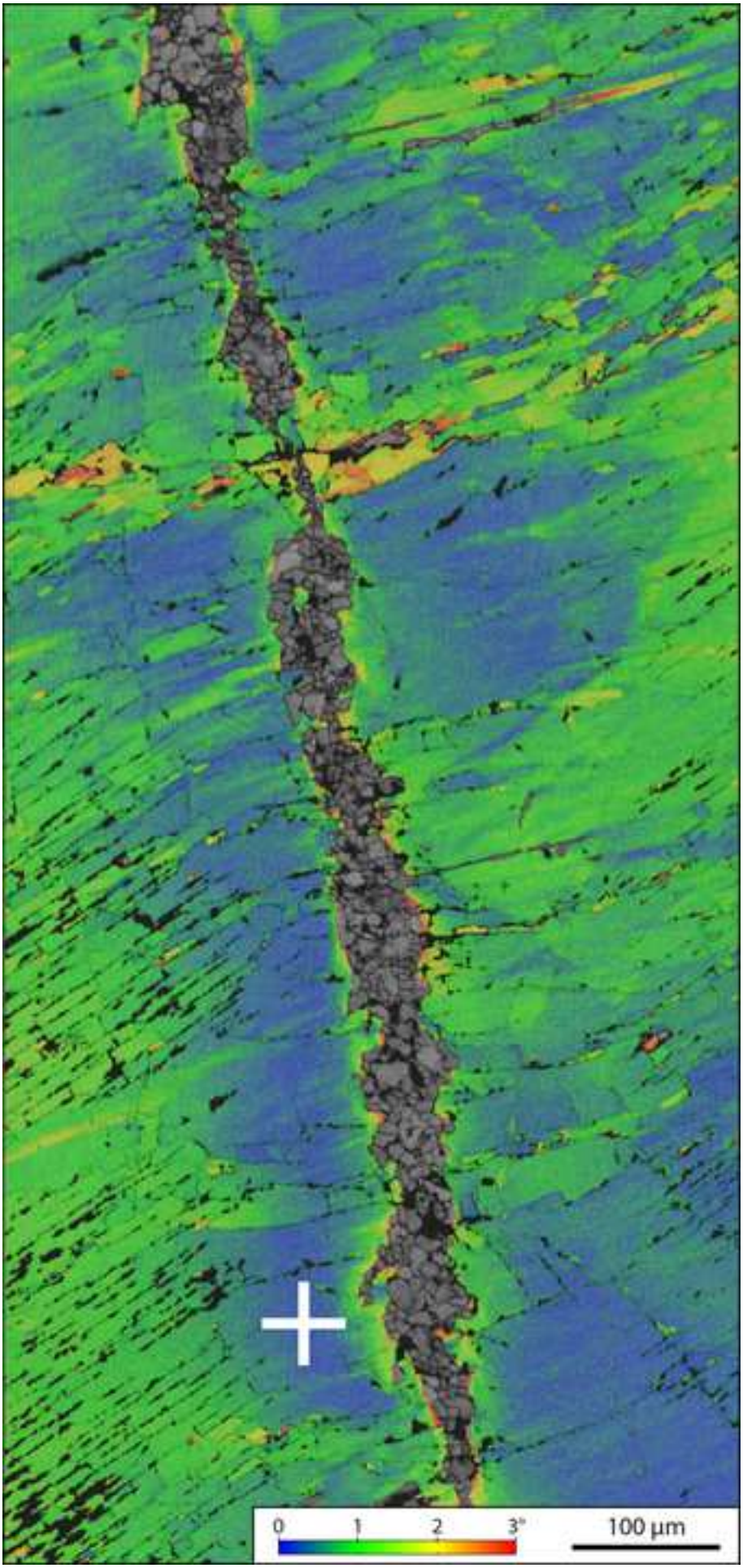

Figure 11

Click here to download Figure Figure 11.tif

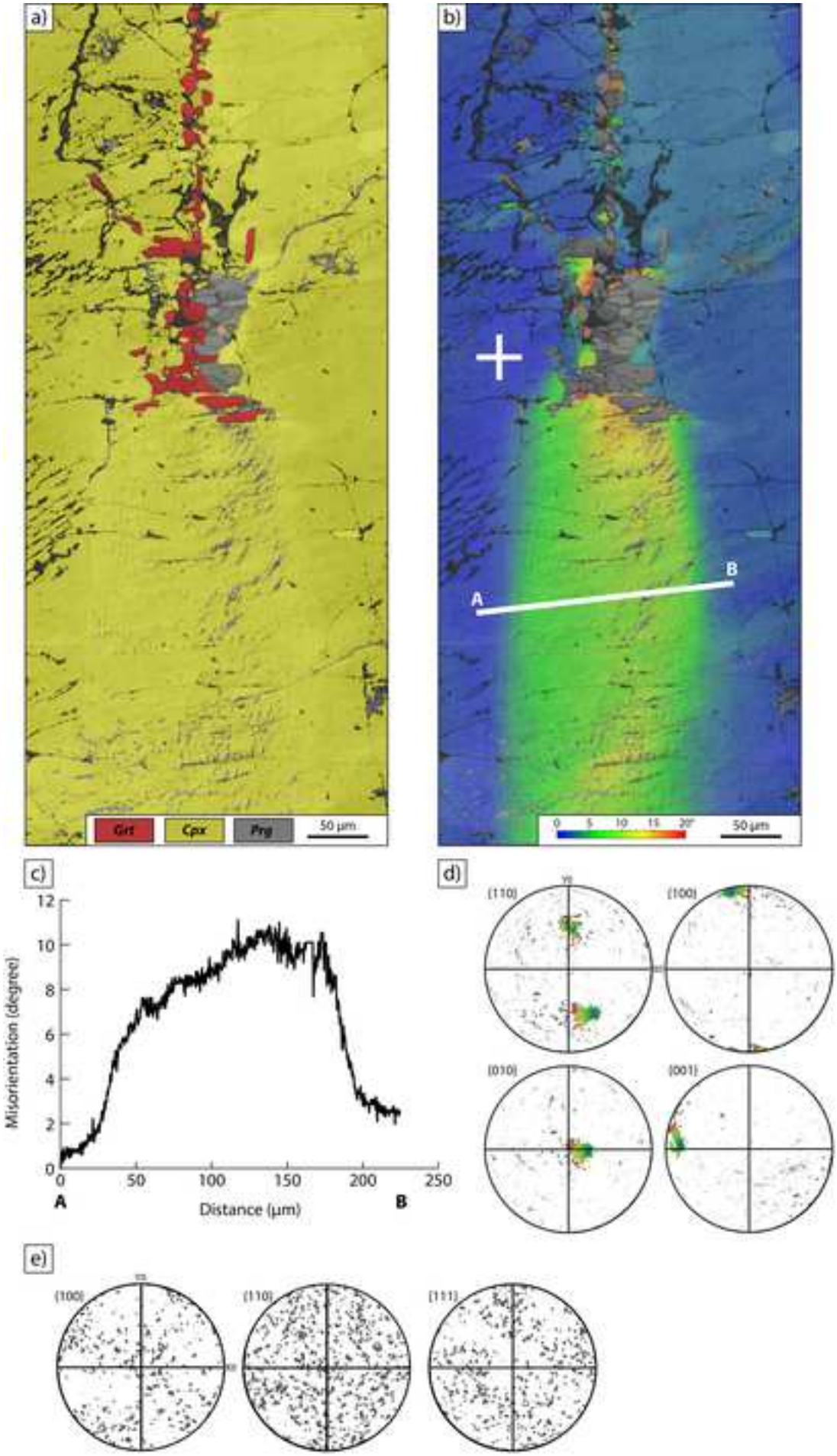

Figure 12



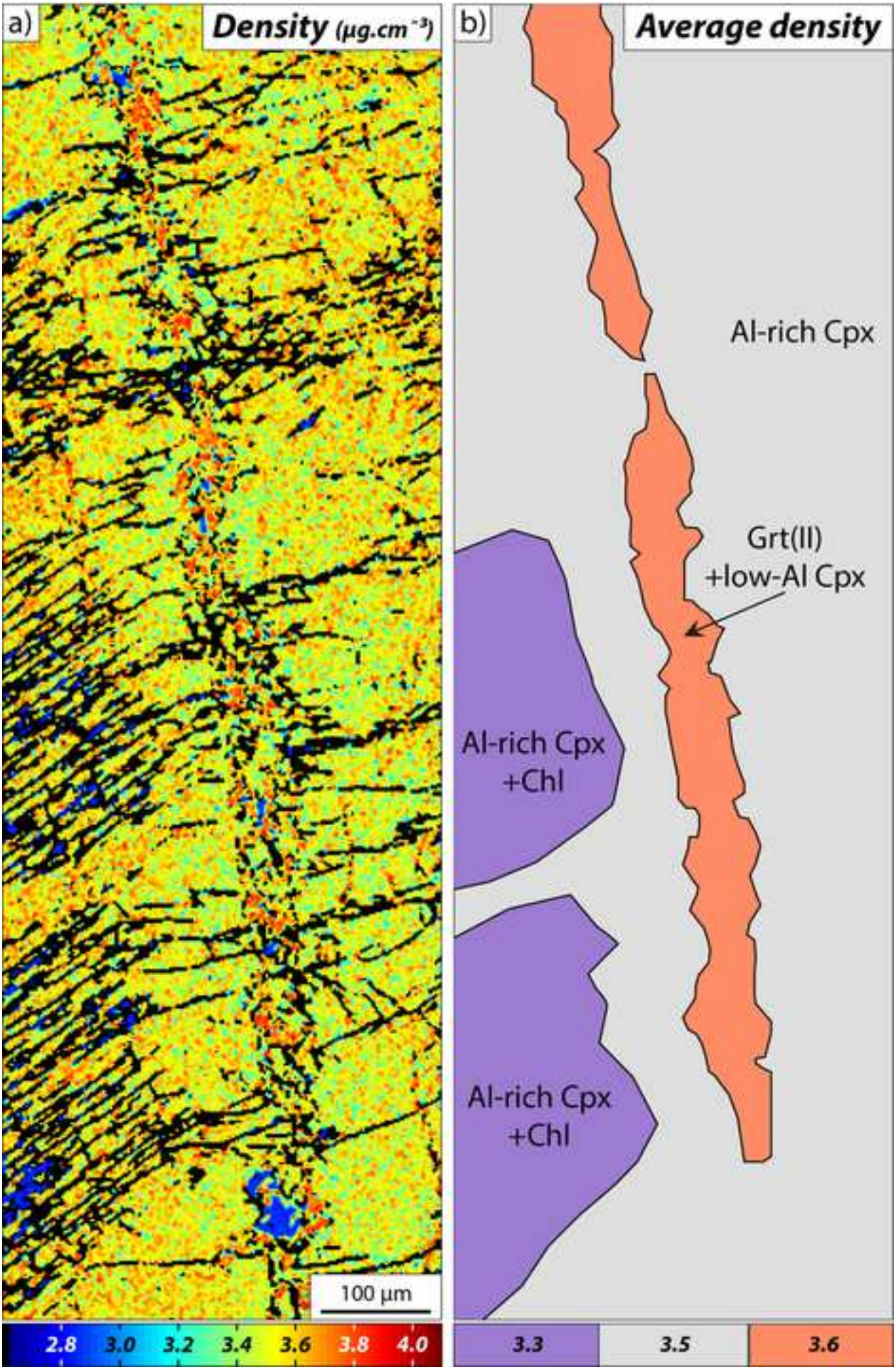

Figure 13

Click here to download Figure Figure 13.tif

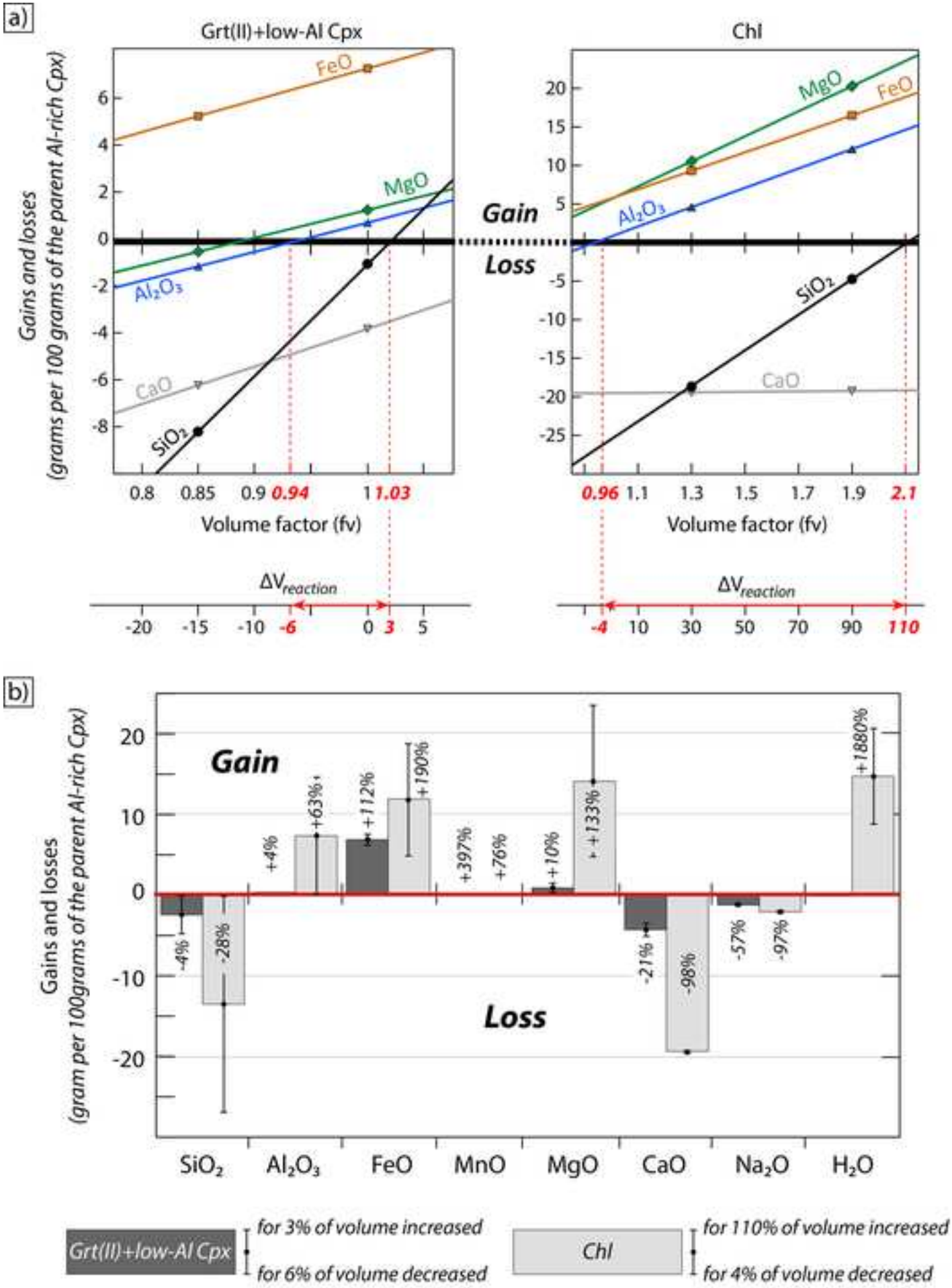

Figure 14

Click here to download Figure Figure 14.tif

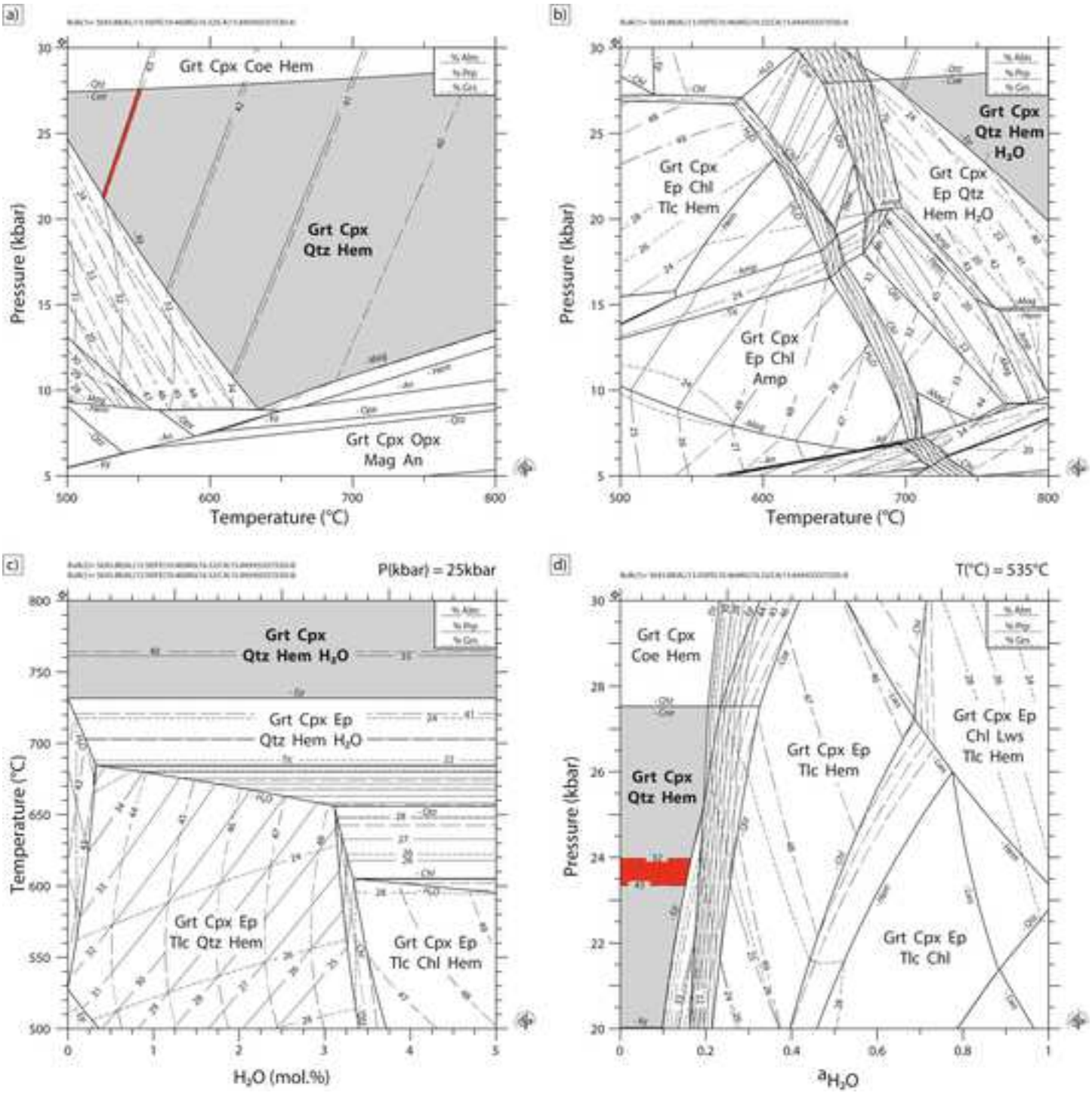

Figure 15

Click here to download Figure Figure 15.tif

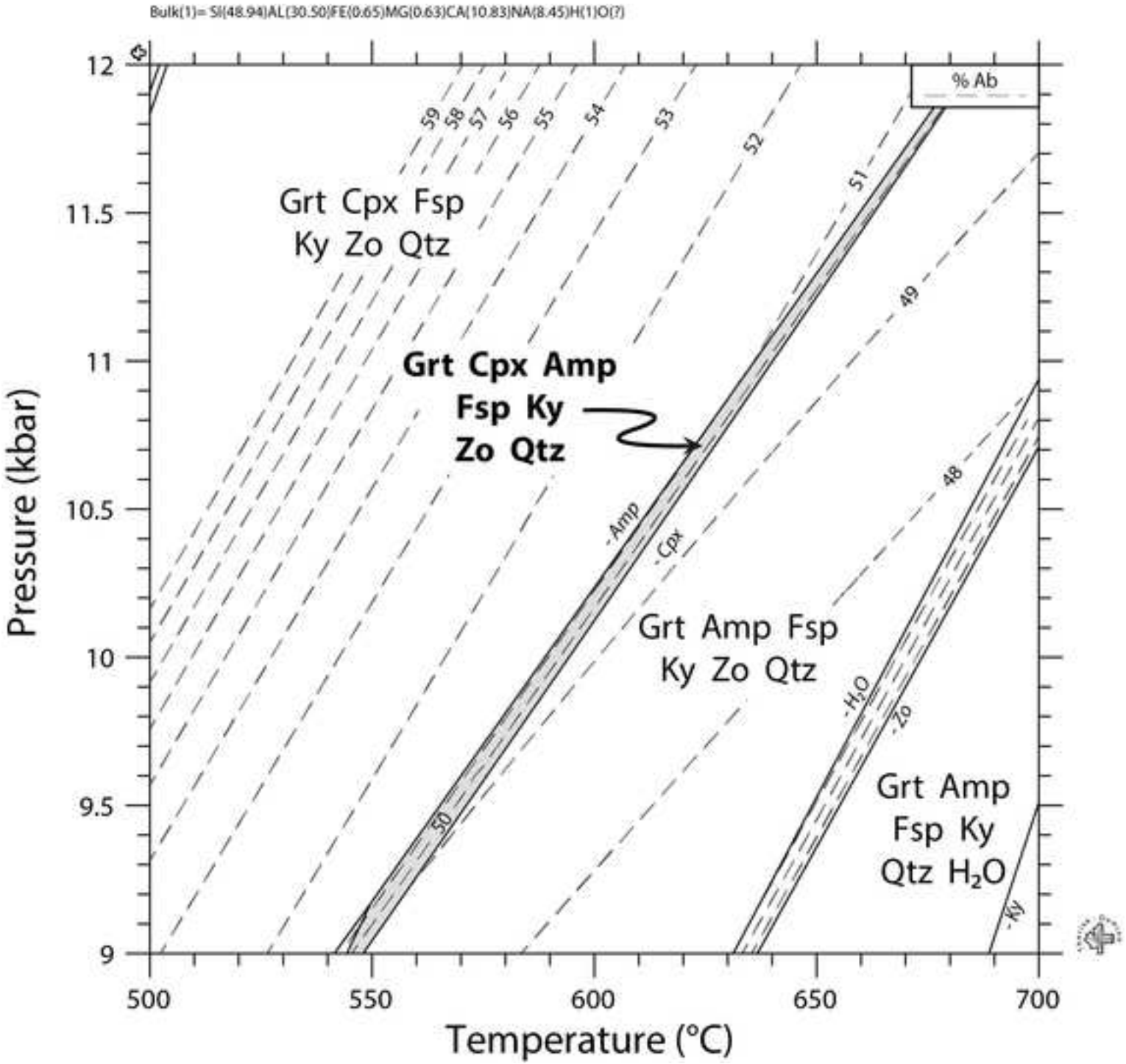

Table 1



| | Garnet | | | | | Clinopyroxene | | |
|---|---|---|---|---|---|---|---|---|
| Analyses | 72 | 73 | 82 | 85 | 90 | 558 | 561 | 566 |
| $SiO_2$ | 40.03 | 40.19 | 38.34 | 39.20 | 38.96 | 48.96 | 49.72 | 53.11 |
| $TiO_2$ | 0.06 | 0.06 | 0.06 | 0.02 | 0.07 | 0.36 | 0.33 | 0.08 |
| $Al_2O_3$ | 22.37 | 22.19 | 21.65 | 21.73 | 21.71 | 11.20 | 11.08 | 3.51 |
| $Cr_2O_3$ | 0.00 | 0.00 | 0.00 | 0.00 | 0.00 | 0.00 | 0.01 | 0.01 |
| $Fe_2O_3$ | 0.75 | 1.71 | 3.29 | 1.65 | 2.36 | 3.53 | 3.98 | 3.96 |
| FeO | 16.31 | 15.57 | 18.92 | 19.00 | 18.27 | 3.67 | 2.51 | 1.97 |
| MnO | 0.38 | 0.33 | 0.33 | 0.31 | 0.31 | 0.07 | 0.06 | 0.05 |
| MgO | 11.70 | 12.21 | 7.61 | 8.24 | 8.36 | 10.44 | 10.76 | 14.02 |
| CaO | 8.10 | 8.15 | 10.21 | 10.07 | 10.28 | 20.24 | 19.82 | 21.81 |
| $Na_2O$ | 0.00 | 0.00 | 0.00 | 0.00 | 0.00 | 2.27 | 2.70 | 1.86 |
| $K_2O$ | 0.00 | 0.00 | 0.00 | 0.00 | 0.00 | 0.02 | 0.03 | 0.00 |
| Totals | 99.71 | 100.42 | 100.42 | 100.22 | 100.31 | 100.75 | 101.00 | 100.39 |
| | Normalized to 12 oxygens: | | | | | Normalized to 6 oxygens: | | |
| Si | 2.990 | 2.979 | 2.927 | 2.978 | 2.957 | 1.782 | 1.796 | 1.934 |
| Ti | 0.004 | 0.003 | 0.004 | 0.001 | 0.004 | 0.010 | 0.009 | 0.002 |
| Al | 1.970 | 1.939 | 1.949 | 1.946 | 1.943 | 0.481 | 0.472 | 0.151 |
| Cr | 0.000 | 0.000 | 0.000 | 0.000 | 0.000 | 0.000 | 0.000 | 0.000 |
| $Fe^{3+}$ | 0.042 | 0.095 | 0.189 | 0.094 | 0.135 | 0.097 | 0.108 | 0.109 |
| $Fe^{2+}$ | 1.019 | 0.965 | 1.208 | 1.207 | 1.160 | 0.112 | 0.076 | 0.060 |
| Mn | 0.024 | 0.021 | 0.022 | 0.020 | 0.020 | 0.002 | 0.002 | 0.002 |
| Mg | 1.303 | 1.349 | 0.866 | 0.933 | 0.946 | 0.566 | 0.579 | 0.761 |
| Ca | 0.648 | 0.647 | 0.835 | 0.820 | 0.836 | 0.789 | 0.767 | 0.851 |
| Na | 0.000 | 0.000 | 0.000 | 0.000 | 0.000 | 0.160 | 0.189 | 0.131 |
| K | 0.000 | 0.000 | 0.000 | 0.000 | 0.000 | 0.001 | 0.001 | 0.000 |
| Sum | 8 | 8 | 8 | 8 | 8 | 4 | 4 | 4 |
| Prp (%) | 44 | 45 | 30 | 31 | 32 | | | |
| Alm (%) | 34 | 32 | 41 | 41 | 39 | | | |
| Sps (%) | 1 | 1 | 0.7 | 0.7 | 0.7 | | | |
| Grs (%) | 26 | 24 | 19 | 23 | 22 | | | |
| Adr (%) | 2 | 5 | 9 | 5 | 8 | | | |

| | | Chlorite | | Amphibole (Pargasite) | |
|---|---|---|---|---|---|
| 576 | 577 | 543 | 551 | 3 | 4 |
| | | | | | |
| 54.23 | 53.15 | 29.89 | 30.18 | 43.50 | 43.36 |
| 0.13 | 0.16 | 0.00 | 0.04 | 0.50 | 0.56 |
| 2.58 | 4.62 | 18.27 | 17.90 | 15.28 | 15.07 |
| 0.00 | 0.00 | 0.00 | 0.02 | 0.00 | 0.00 |
| 1.35 | 0.65 | 0.00 | 0.00 | 2.99 | 2.68 |
| 4.02 | 5.25 | 15.38 | 14.38 | 9.20 | 9.95 |
| 0.04 | 0.02 | 0.07 | 0.06 | 0.15 | 0.15 |
| 14.43 | 13.31 | 22.65 | 23.67 | 12.44 | 12.53 |
| 22.54 | 21.42 | 0.28 | 0.39 | 10.45 | 11.00 |
| 1.36 | 1.55 | 0.01 | 0.01 | 3.37 | 3.38 |
| 0.00 | 0.02 | 0.01 | 0.00 | 0.00 | 0.00 |
| | | | | | |
| 100.68 | 100.15 | 86.55 | 86.66 | 99.63 | 99.31 |
| | | | | | |
| | | N. to 14 oxygens: | | N. to 23 oxygens: | |
| | | | | | |
| 1.971 | 1.943 | 3.009 | 3.020 | 6.293 | 6.255 |
| 0.004 | 0.004 | 0.000 | 0.003 | 0.054 | 0.061 |
| 0.111 | 0.199 | 2.168 | 2.112 | 2.606 | 2.564 |
| 0.000 | 0.000 | 0.000 | 0.002 | 0.000 | 0.000 |
| 0.037 | 0.018 | 0.000 | 0.000 | 0.326 | 0.291 |
| 0.122 | 0.160 | 1.295 | 1.204 | 1.113 | 1.201 |
| 0.001 | 0.001 | 0.006 | 0.005 | 0.018 | 0.018 |
| 0.782 | 0.725 | 3.398 | 3.530 | 2.683 | 2.693 |
| 0.878 | 0.839 | 0.030 | 0.042 | 1.621 | 1.700 |
| 0.096 | 0.110 | 0.001 | 0.003 | 0.945 | 0.947 |
| 0.000 | 0.001 | 0.001 | 0.000 | 0.000 | 0.000 |
| | | | | | |
| 4 | 4 | 9.908 | 9.921 | 15.66 | 15.73 |
| | | | | | |
| | | $X_{Mg}$ 0.72 | 0.75 | | |

Table 2



| | Al-rich Cpx | Grt(II)+low-Al Cpx | Chl |
|---|---|---|---|
| Density | 3.5 | 3.6 | 2.6 |
| $SiO_2$ | 48.58 | 46.04 | 30.97 |
| $TiO_2$ | 0.04 | 0.08 | 0.01 |
| $Al_2O_3$ | 11.71 | 12.02 | 16.83 |
| $Cr_2O_3$ | 0.01 | 0.01 | 0.01 |
| FeO | 6.27 | 13.12 | 16.08 |
| MnO | 0.03 | 0.16 | 0.05 |
| MgO | 10.62 | 11.49 | 21.83 |
| CaO | 19.83 | 15.51 | 0.42 |
| $Na_2O$ | 2.13 | 0.90 | 0.06 |
| $K_2O$ | 0.01 | 0.02 | 0.02 |
| Totals | 99.23 | 99.35 | 86.28 |